127
7-12-76

Dr-199

UCRL-52071

TIME-DEPENDENT PROPAGATION OF HIGH-ENERGY LASER BEAMS THROUGH THE ATMOSPHERE: II

J. A. Fleck, Jr.
J. R. Morris
M. D. Feit

May 18, 1976

Prepared for U.S. Energy Research & Development Administration under contract No. W-7405-Eng-48

Printed in the United States of America
Available from
National Technical Information Service
U.S. Department of Commerce
5285 Port Royal Road
Springfield, VA 22161
Price: Printed Copy $; Microfiche $2.25

Page Range	Domestic Price	Page Range	Domestic Price
001–025	$ 3.50	326–350	10.00
026–050	4.00	351–375	10.50
051–075	4.50	376–400	10.75
076–100	5.00	401–425	11.00
101–125	5.25	426–450	11.75
126–150	5.50	451–475	12.00
151–175	6.00	476–500	12.50
176–200	7.50	501–525	12.75
201–225	7.75	526–550	13.00
226–250	8.00	551–575	13.50
251–275	9.00	576–600	13.75
276–300	9.25	601–up	*
301–325	9.75		

*Add $2.50 for each additional 100 page increment from 601 to 1,000 pages: add $4.50 for each additional 100 page increment over 1,000 pages.

Distribution Category
UC-34

LAWRENCE LIVERMORE LABORATORY
University of California Livermore, California 94550

UCRL-52071

TIME-DEPENDENT PROPAGATION OF HIGH-ENERGY LASER BEAMS THROUGH THE ATMOSPHERE: II

J. A. Fleck, Jr.
J. R. Morris
M. D. Feit

MS. date: May 18, 1976

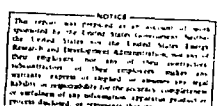

Foreword

This work was done under contract to the U. S. Navy, the Army Missile Command, Huntsville, Alabama, and the U.S. Energy Research and Development Administration.

Contents

TIME-DEPENDENT PROPAGATION OF HIGH-ENERGY LASER BEAMS THROUGH THE ATMOSPHERE: II

Abstract

Various factors that can affect thermal blooming in stagnation zones are examined, including stagnation-zone motion, longitudinal air motion in the neighborhood of the stagnation zone, and the effects of scenario noncoplanarity. Of these effects, only the last offers any reasonable hope of reducing the strong thermal blooming that normally accompanies stagnation zones; in particular, noncoplanarity should benefit multipulse more than cw beams. The methods of treating nonhorizontal winds hydrodynamically for cw and multipulse steady-state sources are discussed. Pulse "self-blooming" in the triangular pulse approximation is discussed in the context of both single and multipulse propagation. It is shown that self-blooming and multipulse blooming cannot be treated independently.

1. Introduction

This is the second report in a series dealing with the general problem of time-dependent thermal blooming of multipulse and cw laser beams.[1] Time dependence is essential for describing the propagation of laser beams through stagnation zones, which are created whenever the motion of the laser platform and the slewing of the laser beam combine to create a null effective transverse wind velocity at some location along the propagation path. The location of vanishing transverse wind we shall call the stagnation point, and the term stagnation zone will refer to the portion of the propagation path, extending in both directions from the stagnation point, where the transverse wind has not yet had time to blow completely across the beam. The lack of wind at the stagnation point creates a steadily decreasing density and a thermal lens whose strength grows with time. This report will continue the study of stagnation

zones begun in Ref. 1, and discuss contributions of self-blooming to multipulse thermal blooming and new models that have been added to the Four-D code.

Both pivoted-absorption-cell measurements[2,3] and detailed numerical calculations of the experimental arrangements[1,4] give evidence that the blooming effects of stagnation zones tend to saturate with time. Thus the beam characteristics seem to approach a kind of quasi-steady state, which is possibly a result of the steady reduction in length of the stagnation zone with time.[3] Despite the existence of these quasi-steady states, calculations for high-power beams show that stagnation zones can lead to severe beam degradation.

The notion of a stagnation zone requires that the transverse wind velocity vanish at at least one position along the propagation path. There are always present, however, a number of additional effects that will prevent a completely stagnant wind condition from occurring at any position. These effects are:

1. Natural convection
2. Motion of the stagnation point with time
3. Longitudinal air motion at the stagnation point
4. Vertical air motion due to noncoplanar scenario geometry

A realistic appraisal of the influence of stagnation zones on beam propagation requires that each of these effects be assessed and possibly incorporated into the computational model.

Natural convection flow at the stagnation point should be negligible for practical beam sizes. A 3.8-μm wavelength and a 474-kW beam power, for example, give a natural convection velocity of the order of 10 cm/s.[1] For this flow velocity and a beam radius of 10 cm at the stagnation point, approximately 2 s is required for the beam to approach a steady-state density distribution. This time is excessive for preventing or reducing stagnation-zone blooming effects, which may develop in times ranging from 1 ms to 0.1 s. At a 10.6-μm wavelength the laser heating rate of the atmosphere is somewhat greater for the same intensity, but the natural convection velocity scales only with the cube root of the absorbed power, so flow velocities would not be significantly above those for the 3.8-μm case. Therefore, we shall not consider the effects of natural convection further.

Under most conditions the stagnation point is not stationary but moves in the same general direction as the target with a velocity that is little different from the

target's. The parcel of air that sees a null wind speed changes with time and thus does not heat up in the manner of a stationary parcel. The influence of this stagnation-point motion on beam propagation was found to be minimal for a cw waveform example treated in Ref. 1. Stagnation-point motion also turns out to be unimportant for a multipulse scenario examined in this report. The conclusion is that stagnation-point motion is unlikely to have much, if any, effect in alleviating stagnation-zone blooming, since, despite the motion, a substantial propagation path exists over which wind velocities are negligible.

The existence of a null transverse wind-velocity component at a stagnation point in no way guarantees a vanishing magnitude of the wind vector, because a nonvanishing longitudinal component almost always exists there. Any air parcel found within the beam at the stagnation point will, as a result, exit from the beam in a finite length of time. Indeed, in coplanar geometries all wind-flow trajectories should cross the beam in two locations: one for values of z (longitudinal position) below the stagnation point z_s, and the other for values above z_s. The wind flow may be in either the positive- or negative-z direction. In the neighborhood of the stagnation point, the wind-flow trajectories will enter one side of the beam, reverse direction with the beam, and exit on the same side.[5] The residence time in the beam for fluid parcels passing through the beam center at the stagnation point will, of course, depend on scenario parameters, but for some typical beam sizes and scenarios this time can be of the order of 0.5 to 1 s. Longitudinal flow should thus be as effective as natural convection in controlling density changes at the stagnation point. One consequence of these re-entrant wind-flow trajectories is that air densities for z values greater than z_s could be influenced hydrodynamically by densities for z values less than z_s; but, for any foreseeable practical scenarios, the re-entrant times — except perhaps in the immediate neighborhood of the stagnation point — would be considerably longer than times of interest. Consequently, hydrodynamic coupling between points above and below z_s can be safely neglected in cases of practical interest.

The existence of a position where the transverse wind velocity vanishes presupposes the extremely improbable coplanarity of the laser beam and the trajectories of its platform and the target — a situation that is clearly a limiting case of real-world

scenarios, which are invariably noncoplanar. In the more general case of noncoplanar geometry, only the wind component along a certain transverse axis can be expected to vanish. The wind vector in the transverse plane will rotate and attain its minimum magnitude at the stagnation point. Since this minimum magnitude can never vanish, except in a space of measure zero, a steady state can always be defined for the governing hydrodynamic equations. The significance of this is that, in systems analysis, steady-state numbers can always be assigned to stagnation-zone situations, at least for some nominal degree of noncoplanarity, and these numbers can be obtained from simple and relatively cheap steady-state calculations. Truly coplanar stagnation-zone situations, in contrast, require time-dependent calculations that are expensive and require considerable care in execution.

In the coplanar scenario described in Ref. 1, for example, if the laser is given an elevation of 10 m above the plane containing the target and the laser platform, the vertical component of wind velocity at the stagnation point takes on the value of 1 m/s. This is sufficient to establish a steady state in a time of the order of 0.1 s, which is short compared to times of interest. The small vertical velocity component at the stagnation point leads to substantial changes in isointensity contours in the focal plane, but the average intensity is remarkably close to the quasi-steady-state value obtained in a time-dependent calculation for the corresponding coplanar case.

Thus, small amounts of noncoplanarity should not be expected to greatly improve cw laser performance in stagnation-zone situations but should contribute to ease in understanding and predicting it. The case of multipulse beams is another matter. As pulse-repetition frequencies are lowered, a small vertical wind component at the stagnation point becomes more and more effective in sweeping out the air between pulses. The benefits of noncoplanarity in stagnation-zone situations should thus be greater for multipulse beams than for cw beams.

The current status of the Four-D code is summarized in Table 1, and recent additions to the code are described in the body of this report. We have continued to adhere to the philosophy that the best way to approach all laser-propagation calculations is through a single, unified computer code that can be applied to any problem. The advantages of this are threefold. First, it greatly simplifies bookkeeping (or,

more appropriately, code-keeping), since a proliferation of limited special-purpose codes is avoided. Second, if each type of calculation is made a subset of a larger calculational capability, new features added to the code — such as data-processing routines, adaptive-lens transformations, scenario features, etc. — are available to all types of calculation at once. Third, realistic simulations are possible, since a wide range of conditions can be incorporated into any calculation.

Table 1. Basic outline of current Four-D propagation code.

Variables	x, y, z, t, where x, y are transverse coordinates and z is axial displacement.
Form of propagation equation	Scalar wave equation in parabolic approximation $$2ik\frac{\partial \mathcal{E}}{\partial z} = \nabla_\perp^2 \mathcal{E} + k^2(n^2 - 1)\mathcal{E} \ .$$
Method of solving propagation equation	Symmetrized split operator, finite Fourier series, fast Fourier transform (FFT) algorithm $$\mathcal{E}^{n+1} = \exp\left(-\frac{i\Delta z}{4k}\nabla_\perp^2\right)\exp\left(-\frac{i\Delta z}{2k}\chi\right)\exp\left(-\frac{i\Delta z}{4k}\nabla_\perp^2\right)\mathcal{E}^n$$ $$\chi = k^2(n^2 - 1) \ .$$
Hydrodynamics for steady-state cw problems	Uses exact solution to linear hydrodynamic equations. Fourier method for M < 1. Characteristic method for M > 1. Solves $$v_x\frac{\partial \rho_1}{\partial x} + v_y\frac{\partial \rho_1}{\partial y} + \rho_0\,\underline{\nabla}_\perp \cdot \underline{v}_\perp = 0,$$ $$\rho_0\left(v_x\frac{\partial v_1}{\partial x} + v_y\frac{\partial v_1}{\partial y}\right) + \underline{\nabla}_\perp p_1 = 0,$$ $$\left(v_x\frac{\partial}{\partial x} + v_y\frac{\partial}{\partial y}\right)\left(p_1 - \sigma_s^2\rho_1\right) = (\gamma - 1)\alpha I.$$
Transonic slewing	Steady-state calculation valid for all Mach numbers except M = 1. Code can be used arbitrarily close to M = 1.

Table 1 (continued).

Treatment of stagnation-zone problems for cw beams	Time-dependent isobaric approximation. Transient succession of steady-state density changes; i.e., solves $$\frac{\partial \rho_1}{\partial t} + v \frac{\partial \rho_1}{\partial x} = - \frac{\gamma - 1}{c_s^2} \alpha I \ .$$
Nonsteady treatment of multipulse density changes	Changes in density from previous pulses in train are calculated with isobaric approximation using $$\frac{\partial \rho_1}{\partial t} + v_x \frac{\partial \rho_1}{\partial x} = - \frac{\gamma - 1}{c_s^2} \alpha \sum_n \tau I_n(x,y) \ \delta(t - t_n) \ ,$$ where $\tau I_n(x,y)$ is nth pulse fluence. Density changes resulting from the same pulse are calculated using acoustic equations and triangular pulse shape.
Method of calculating density change for individual pulse in train	Takes two-dimensional Fourier transform of $$\frac{\alpha \tilde{I} t_p}{2c_s^2} \left\{ 1 - \frac{\sin^2 \left[\frac{1}{2} c_s \left(k_x^2 + k_y^2 \right)^{1/2} t_p \right]}{\left[\frac{1}{2} c_s \left(k_x^2 + k_y^2 \right)^{1/2} t_p \right]^2} \right\} ,$$ where $\tilde{I}$ is Fourier transform of intensity, and t_p is the time duration of each pulse. Source aperture should be softened when using this code provision.
Treatment of steady-state multipulse blooming	Previous pulses in train are assumed to be periodic replications of current pulse. Solves $$\frac{\partial \rho_1}{\partial t} + v_x \frac{\partial \rho_1}{\partial x} + v_y \frac{\partial \rho_1}{\partial y} = - \frac{\gamma - 1}{c_s^2} I \sum_n \delta(t - t_n) \ .$$ Pulse self-blooming is treated as in the nonsteady-state case.
Treatment of turbulence	Uses phase-screen method of Bradley and Brown with Von Karman spectrum. Phase screen determined by

Table 1 (continued).

$$\Gamma(x,y) = \int_{-\infty}^{\infty} dk_x \exp(ik_x) \int_{-\infty}^{\infty} dk_y \exp(ik_y) \times a(k_x,k_y)\, \phi_n^{1/2}(k_x,k_y) ,$$

where a is a complex random variable and Φ_n is spectral density of index fluctuations.

Lens transformation and treatment of lens optics

Compensates for a portion of lens phase front with cylindrical Talanov lens transformation. Uses in spherical case

$$\frac{1}{z_f} = \frac{1}{z_T} + \frac{1}{z_L} ,$$

where z_f is focal length of lens, z_T is focal length compensated for by Talanov transformation, and z_L is focal length of initial phase front.

Treatment of nondiffraction limited beams

Spherical-aberration phase determined by

$$\phi^{SA} = \frac{2\pi A}{\sigma^2} (x^2 + y^2)^2 ,$$

or phase-screen method of Hogge *et al.* Phase determined as in turbulence, only

$$\Phi_n = \frac{\sigma^2 l_o^2}{2\pi} \exp\left(-\frac{l_o^2 k^2}{2}\right),$$

where l_o is correlation length and σ^2 phase variance.

Adaptive lens transformation

Removes phase

$$\sum_{i=1}^{2} \left[\alpha_i (x_i - \langle x_i \rangle)^2 + \beta_i (x_i - \langle x_i \rangle)\right]$$

through lens transformation and deflection of beam. Here $x_1 = x$, $x_2 = y$, averages are intensity weighted, α_i and β_i are calculated to keep the intensity centroid at mesh center, and intensity weighted r.m.s. values of x and y are constant with z.

Table 1 (continued).

Selection of z-step	Adaptive z-step selection based on limiting gradients in nonlinear contribution to phase. Constant z-step over any portion of range also possible.
Scenario capability	General noncoplanar scenario geometry capability involving moving laser platform, moving target, and arbitrary wind direction. In coplanar case, wind can be function of t and z.
Treatment of multiline effects	Calculates average absorption coefficient based on assumption of identical field distributions for all lines $$\bar{\alpha} = \frac{\sum_i \alpha_i f_i \exp(-\alpha_i z)}{\sum_i f_i \exp(-\alpha_i z)}$$ where f_i is fraction of energy in line i at $z = 0$.
Treatment of beam jitter	Takes convolution of intensity in target plane with Gaussian distribution: $$I_{\text{jitter}} = \iint \exp\left(-\frac{x'^2 + y'^2}{2\sigma^2}\right) \times I(x - x', y - y')\, dx'\, dy' ,$$ where σ^2 is variance introduced by jitter.
Code output	Isointensity, isodensity, isophase, and spectrum contours. Intensity averaged over contours. Plots of intensity, phase, density, spatial spectrum along specific directions, etc., at specific times. Plots of peak intensity and average intensity vs time.
Numerical capacity when used with CDC 7600 and restricted to internal memory (large and small core)	Spatial mesh, 64 × 64, 35 sampling times, no restriction on number of axial space increments.
Problem zoning features	Number of space increments in x and y directions must be equal and expressible as a power of 2.

2. Treatment of Moving Stagnation Zones in Coplanar Scenarios

The basic coplanar scenario geometry is depicted in Fig. 1. It is assumed that the target and laser platform will collide on the x axis after a time τ_c has elapsed. The point of impact is denoted by P and the position of the laser by L. The effective transverse wind speed V_t is given by the expression

$$V_t(\tau_c, z) = -\sin\theta_T[V_T - \frac{z}{R}(V_T - V_p + V_n \cot\theta_T)] + V_W \sin(\theta_W - \theta_T), \quad (1)$$

where V_R is the target (receiver) velocity, V_T is the laser-platform (transmitter) velocity, V_W is the background wind velocity, R is the

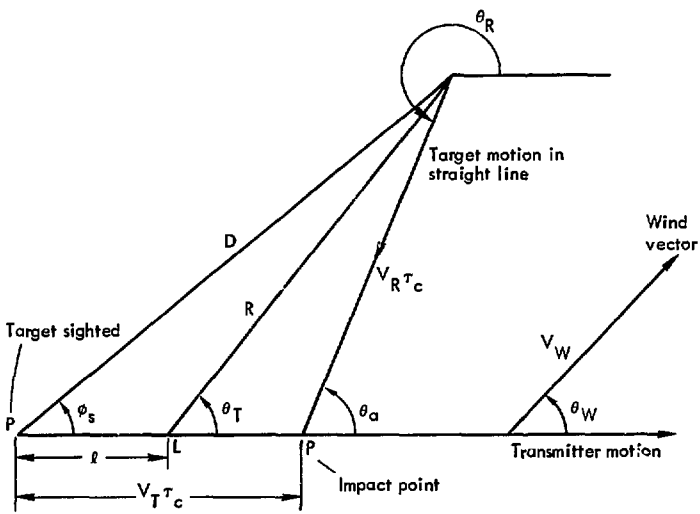

Fig. 1. Diagram of coplanar scenario model.

range,

$$V_p = V_R \cos \theta_R \ , \qquad (2)$$

and

$$V_n = V_R \sin \theta_R . \qquad (3)$$

From simple trigonometry,

$$\theta_T = \cot^{-1}\left[\frac{\cos \theta_a + (V_T\tau_c - z)/V_R\tau_c}{\sin \theta_a}\right] \qquad (4a)$$

$$R = \frac{D \sin \phi_s}{\sin \theta_T} \ , \qquad (4b)$$

where θ_a is constant.

The transverse wind speed V_t depends on τ_c and hence on time through the dependence of the scenario parameters θ_T and R on time in Eqs. (4a) and (4b). The Four-D code is programmed to calculate $V_t(\tau_c, z)$ as a function of τ_c and hence of time. The hydrodynamic equations are solved numerically by assuming that V_t is stepwise constant over each integration time interval Δt.

The location of a stagnation point is determined by setting the right-hand side of Eq. (1) equal to zero. Clearly, that point moves with time, and, as a result, a different parcel of air undergoes heating under conditions of zero wind velocity at each instant. In general the stagnation point will move with a velocity comparable to that of the target. The determination of V_t from Eqs. (1)-(4) for use in the hydrodynamic equations permits an accurate determination of the effect of motion on the thermal lens in the stagnation zone. It is more difficult to follow the irradiance on a moving target, however, since all equations are solved in a retarded time frame. It would be necessary to store the irradiance history for the values of z corresponding to the target motion. Since the relative change of the range R in a time of interest is small, it is a good approximation to assume the focal distance and the range R at which the laser intensity is monitored to be constants in time, while the correct variable R is taken into account in the hydrodynamic portion of the calculation by means of Eqs. (1)-(4).

3. Propagation of Multipulse Laser Beams Through Stagnation Zones

The particular scenario chosen leads to the effective transverse wind as a function of range for $\tau = 0$, shown in Fig. 2, where τ is measured from the time the pulse turns on. The pertinent physical

data are the following:

Power, P	53 kW
Range, R	2.5 km
Focal length, f	4.5 km
Absorption coefficient, α	0.25 km^{-1}
Wavelength, λ	10.6 μm
Aperture diameter, $2a$ (Gaussian at $1/e^2$)	30 cm
Slewing rate, Ω	7.44 mrad/s
Pulse-repetition rate, ν	10, 25, 50, and 100 s^{-1}

These data can be expressed in terms of the following dimensionless numbers:

$$N_F = ka^2/f = 2.96,$$

$$N_O = 2a/v_0\Delta t = 3.2 \times 10^{-2}\nu,$$

$$N_S = \Omega f/v_0 = 3.6,$$

$$N_A = \alpha f = 1.125,$$

$$N_D = \frac{1}{2}\frac{\partial\varepsilon}{\partial\rho}\frac{N_O N_A N_F(\gamma - 1)E_p}{c_s^2 a^3\left(\frac{a}{f}\right)} = 100,$$

where N_F, N_O, N_S, N_A, and N_D represent respectively the Fresnel, overlap, slewing, absorption, and distortion numbers. Although the chosen power, 53 kW, is rather low, the value of the distortion number N_D is quite high, and the resulting thermal blooming is about the maximum that the code can accommodate. In any case, the above parameters

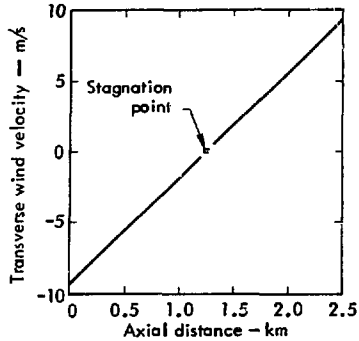

Fig. 2. Transverse wind velocity as a function of axial distance.

are adequate for assessing the sensitivity of typical multipulse laser performance to stagnation-zone motion.

In the present scenario, the stagnation zone and target move with a speed of 300 m/s. For a multipulse beam with $\nu = 100\ s^{-1}$, the stagnation zone moves 3 m between pulses, whereas for $\nu = 10\ s^{-1}$, the stagnation zone moves 30 m between pulses. It would be hoped that, in the case of the lower pulse-repetition frequency, the greater movement of the stagnation zone would lead to a reduced buildup of stagnant-air density changes. This effect turns out to be minimal. The time dependence of the average intensity on target (averaged over the minimum half-power area) is shown for the case of no stagnation-zone motion in Fig. 3(a) and for the

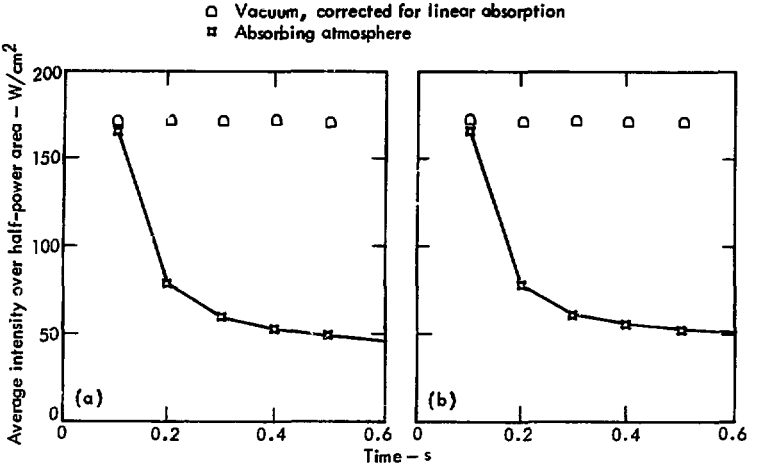

Fig. 3. Area-averaged target intensity as a function of pulse time: six pulses at $\nu = 10\ s^{-1}$. (a) No stagnation-zone motion included. (b) Stagnation-zone motion included.

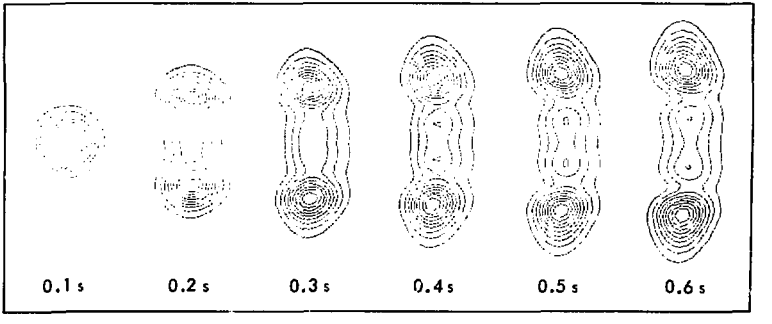

Fig. 4. Isointensity contours as a function of pulse time for $\nu = 10\ s^{-1}$.

Table 2. Comparison of multipulse intensities with and without stagnation-zone motion.

Time (s)	Time-averaged intensity (W/cm^2)			
	No motion		Motion	
	Average	Peak	Average	Peak
0.1	168.5	234.0	168.5	234.0
0.2	78.9	117.3	78.7	117.3
0.3	60.7	100.7	60.8	103.3
0.4	53.7	92.5	55.3	96.8
0.5	49.6	88.7	52.4	92.7
0.6	47.3	84.1	50.2	87.5

Maximum increase resulting from stagnation-zone motion: av, 6.1%; peak, 4.0%.

case with stagnation-zone motion in Fig. 3(b). The calculation is carried out for six pulses. The isointensity contours for the six pulses are shown in Fig. 4 for the moving stagnation zone. The contours in the nonmoving case are so similar that they are not shown. The performance in the two cases is summarized pulse by pulse in Table 2, where the intensity values have been averaged over the interpulse separation time, and the percent improvements in intensity indicated are for the last pulse in the train.

Surprisingly, the improvements in peak and average fluence go in the opposite direction. The peak and average fluences are actually slightly higher in the no-motion case, as shown in Table 3.

This behavior is due to the large contribution that the first pulse in the train makes to the total fluence. The isofluence contours for the case with motion are displayed in Fig. 5. The central fluence peak contains the maximum value and makes the largest contribution to the fluence averaged over the minimum half-power area. Apparently in the no-motion case the subsequent pulses in the train make a greater contribution in the central region than do the corresponding pulses in the case with motion. This small difference in peak and average fluences is of

Table 3. Comparison of fluences with and without stagnation-zone motion.

Fluence (J/cm^2)			
No motion		Motion	
Average	Peak	Average	Peak
30.61	42.1	30.1	40.7

Decrease resulting from stagnation-zone motion: av, 1.7%; peak, 3.3%.

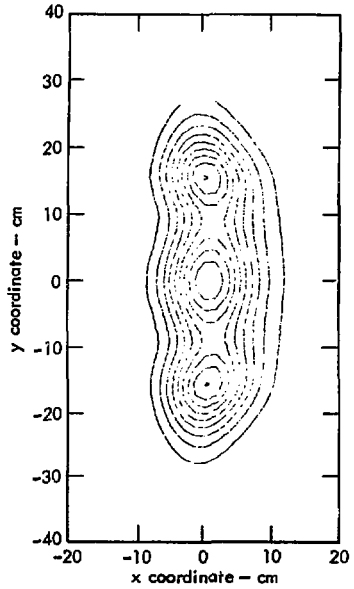

Fig. 5. Fluence contours for case of $\nu = 10\ s^{-1}$, motion included.

little or no practical importance, and is indicative of the fact that stagnation-zone motion plays no vital role in determining thermal blooming in stagnation zones.

Figure 6 shows the dependence of average intensity on time at the target range for different values of pulse-repetition rate, ν. Each curve begins with the time of arrival of the second pulse. (The first pulse would create a time-averaged intensity of 189 W/cm^2.) It is clear that reducing ν diminishes the effect of the stagnation zone. The reason obviously is that for smaller values of ν the air can be swept out by wind between pulses over a greater proportion of the propagation path.

Sample pulse-isointensity contours for $\nu = 100\ s^{-1}$ are displayed in Fig. 7; these should be compared with those for $\nu = 10\ s^{-1}$ in Fig. 4. At the lower repetition rate, the beam has divided into two distinct spots. At the higher rate, lateral peaks are also formed but they are much less distinct. The lateral spreading of the contours as a function of time is shown in Fig. 8. The width perpendicular to the wind

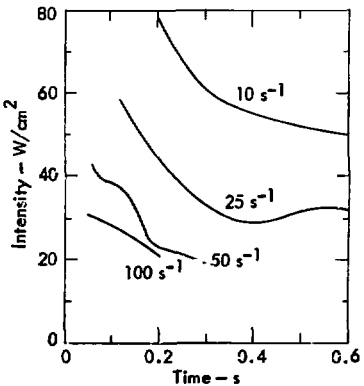

Fig. 6. Space-averaged intensity as a function of pulse time for various pulse-repetition rates.

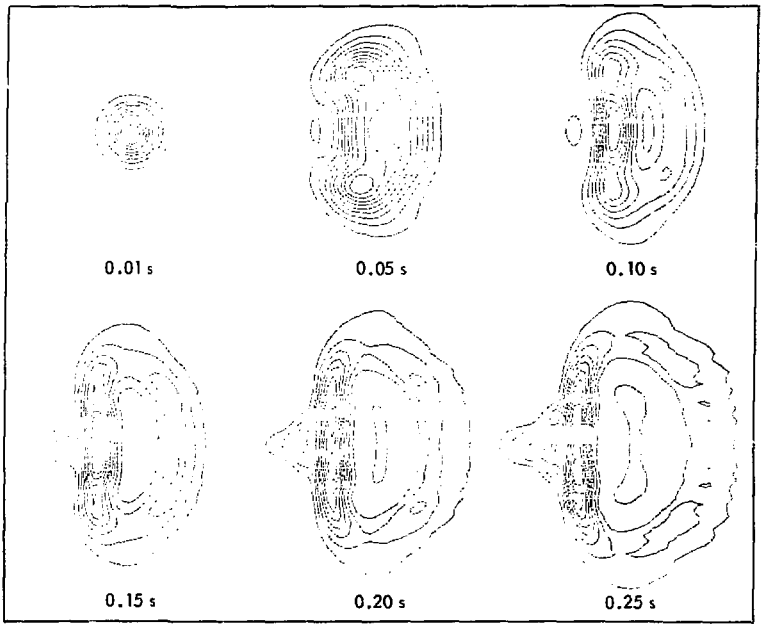

Fig. 7. Isointensity contours for pulses sampled from $\nu = 100\ s^{-1}$ train.

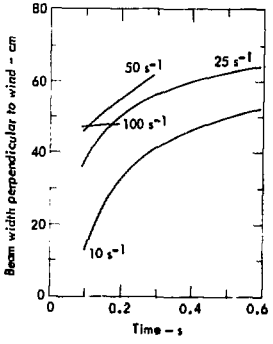

Fig. 8. Width of beam in direction perpendicular to the wind at various pulse-repetition frequencies.

is determined by measuring the maximum distance perpendicular to the wind direction between 30% contours.

In conclusion, the performance of a multipulse laser under stagnation-zone conditions can be improved by lowering the pulse-repetition frequency, but, with or without motion of the stagnation point, the thermal blooming is likely to be substantial.

4. Effect of Longitudinal Air Motion on Flow in the Neighborhood of a Stagnation Zone for Coplanar Scenarios

We wish to examine the air-flow trajectories in a coordinate system that moves with the laser beam. Take the x axis along the direction of motion of the laser platform and the y axis perpendicular to it in the scenario plane. The unit vector $\hat{z}(t)$ is directed along the rotating laser beam, and $\hat{x}'(t)$ is taken normal to $\hat{z}(t)$ (see Fig. 9). At any instant of time, $\hat{z}(t)$ and $\hat{x}'(t)$ can be expressed in the rest frame of the laser platform by means of the relations

$$\hat{z}(t) = [\cos \theta_T(t), \sin \theta_T(t)], \quad (5a)$$

$$\hat{x}'(t) = [\sin \theta_T(t), -\cos \theta_T(t)], \quad (5b)$$

where

$$\theta_T = \cos^{-1}(\hat{z} \cdot \hat{z}), \quad (6)$$

and the angle θ_T is calculated from the scenario Eq. (4a) by substituting $\tau_o - t$ for τ_o. The common origin for the rest frames of the laser platform and the rotating laser beam will be taken at the center of the laser aperture.

The effective wind vector in the moving coordinate system of the laser can be expressed as

$$\underline{V}_{eff} = \underline{V}_{rel} - \frac{(\underline{V}_R - \underline{V}_T)}{R(t)} \cdot \hat{x}' \times [z(t)\,\hat{x}'(t) - x'(t)\,\hat{z}(t)]. \quad (7)$$

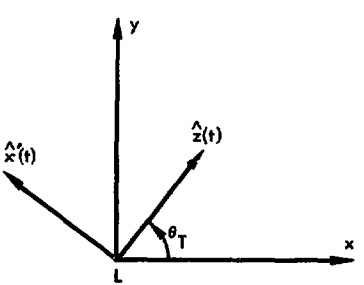

Fig. 9. Vector diagram in scenario plane; $\hat{z}(t)$ indicates instantaneous direction of slewing laser beam.

Here $\underline{V}_R$ is the target velocity relative to the earth's surface, and

$$\underline{V}_{rel} = \underline{V}_w - \underline{V}_T \ , \qquad (8)$$

where $\underline{V}_T$ is the velocity of the laser platform and $\underline{V}_w$ is the velocity of the wind. An air test particle will move in the rest frame of the laser platform along trajectories described by

$$\underline{r}(t) = \underline{r}(0) + \underline{V}_{rel} t \ . \qquad (9)$$

These trajectories can be expressed in the rotating frame of the laser beam by means of the following relations:

$$x'(t) = \underline{r}(t) \cdot \hat{x}'(t), \qquad (10a)$$

$$z(t) = \underline{r}(t) \cdot \hat{z}(t) \ . \qquad (10b)$$

Figure 10 shows sample air-particle trajectories in the vicinity of a stagnation point for four different scenarios of practical interest (of the type shown in Fig. 1). The target range and stagnation point location at $t = 0$ are indicated in Table 4. At time $t = 0$ the particles are assumed to be located precisely at the stagnation point. The origin of the transverse coordinate is assumed to be at the center of the beam. The ticks on the trajectories indicate points separated by 0.5 s in time. The arrows indicate the direction of air flow with increasing time. Also shown in Table 4 are the times τ actually spent in the laser beam by a particle that crosses the stagnation point at the center of a 10-cm-radius beam.

The longitudinal wind speed in the neighborhood of the stagnation point is roughly equal to $\underline{V}_{rel}$, as can be seen from Eq. (7). For the scenarios described in Table 4, $\underline{V}_{rel}$ is of the order of 10 m/s. For these scenarios the longitudinal wind component will be of limited value in clearing the beam in the vicinity of the stagnation point.

Table 4. Residence time in beam for air particles passing through stagnation point.

Scenario	Target position at $t = 0$ (km)	Stagnation point at $t = 0$ (km)	Residence time, τ (s)
A	1.5	0.844	1.0
B	1.0	0.379	0.5
C	2.5	2.33	1.7
D	1.0	0.295	1.0

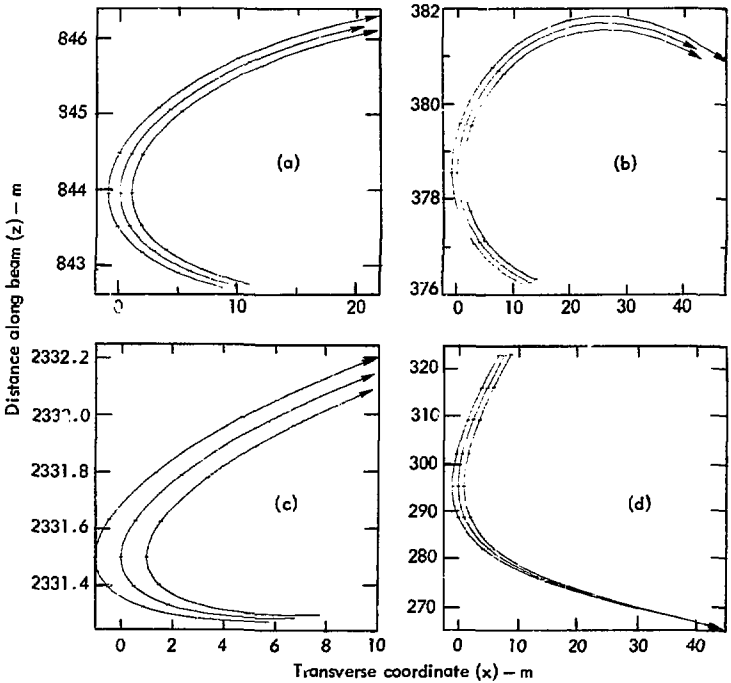

Fig. 10. Air-flow trajectories in rest frame of slewing laser beam in the presence of a stagnation zone. Ticks on the curves denote 0.5-s intervals. (a) Range = 1.5 km, stagnation point at z = 0.844 km. (b) Range = 1.0 km, stagnation point at z = 0.379 km. (c) Range = 2.5 km, stagnation point at z = 2.33 km. (d) Range = 1 km, stagnation point at z = 0.295 km.

5. Calculation of Transverse Wind Velocities for Noncoplanar Scenarios

We shall again assume the scenario of Fig. 1, only now we shall relax the assumption that the scenario or kinematic plane necessarily coincides with the earth's, or the horizontal, plane. The line *PLP* and the wind vector, however, will be assumed to lie in the earth's plane (see Fig. 11). Again, the x direction will be along the direction

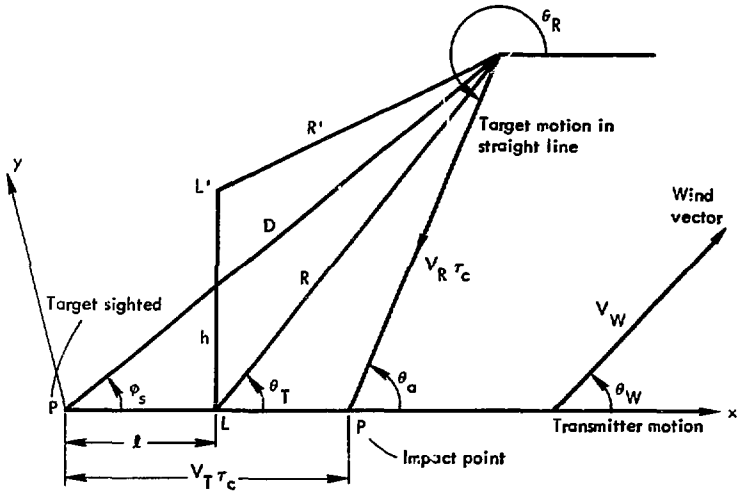

Fig. 11. Diagram of noncoplanar scenario. Laser is now situated at a height h above the platform.

of motion of the laser platform, the y direction will be in the kinematic plane, and the unit vector normal to the kinematic plane will be called $\hat{\zeta}$. The laser aperture will be situated at position L', which is at a height h abov the line PLP. The line LL' defines the vector $\underline{h} = \underline{h} = h\hat{h}$, which is normal to the horizontal plane and makes an angle θ_p with the vector $\hat{\zeta}$. The scenario parameters D, Φ_s, R, θ_R, ℓ, and θ_T are now defined in a plane tilted with respect to the horizontal plane, but they are related exactly the same as before. The distance R, however, no longer has the significance of range. The calculation of the true range R' is described below.

In order to follow the wind in a frame of reference that moves with the laser, it is necessary to introduce an appropriate orthogonal coordinate system. Clearly this coordinate system will not be unique, but a suitable one can be defined as follows: $\hat{x}$ is directed along the laser beam,

$$\hat{y}' = \frac{\hat{x} \times \underline{V}_T}{|\hat{x} \times \underline{V}_T|}, \qquad (11a)$$

and

$$\hat{z}' = \hat{y}' \times \hat{x} . \qquad (11b)$$

It is most convenient to express all vectors used in the computation in

the kinematic coordinate system. Hence we have

$$\hat{V}_T = (1, 0, 0) , \tag{12a}$$

$$\hat{V}_R = (\cos\theta_R, \sin\theta_R, 0), \tag{12b}$$

$$\hat{R} = (\cos\theta_T, \sin\theta_T, 0), \tag{12c}$$

$$\hat{h} = (0, \sin\theta_p, \cos\theta_p), \tag{12d}$$

$$\hat{V}_W = (\cos\theta_W, \sin\theta_W \cos\theta_p, - \sin\theta_W \sin\theta_p) \tag{12e}$$

$$\underline{R}' = \underline{R} - \underline{h} , \tag{12f}$$

where $\hat{V}_T$, $\hat{V}_R$, $\hat{V}_W$ are unit vectors directed along $\underline{V}_T$, $\underline{V}_R$, and $\underline{V}_W$, and the vectors $\underline{R} = R\hat{R}$ and $\underline{R}'$ are directed along lines extending from L and L', respectively, to the receiver (target).

The effective wind seen in the frame of reference moving with the laser beam is

$$\underline{V}_{eff}(z,t) = (\underline{V}_W - \underline{V}_T) - \frac{z}{R'}\left\{[\underline{V}_R - (\underline{V}_R \cdot \hat{z})\hat{z}] - [\underline{V}_T - (\underline{V}_T \cdot \hat{z})\hat{z}]\right\}. \tag{13}$$

The effective wind components along $\hat{x}'$ and $\hat{y}'$ are then obtained from

$$V_{effx'} = \underline{V}_{eff} \cdot \hat{x}' , \tag{14a}$$

$$V_{effy'} = \underline{V}_{eff} \cdot \hat{y}' . \tag{14b}$$

The effective horizontal and vertical wind components in Eqs. (14) become inputs to the hydrodynamic calculation which is described in Sections 6 and 7.

6. Steady-State Solutions of Hydrodynamic Equations for Arbitrary Transverse Wind Velocities: cw Steady State

Noncoplanar scenarios create effective winds whose orientation in the transverse plane vary with propagation distance z. All symmetry in the transverse plane is lost, and the x axis can no longer serve as the wind axis. The linearized hydrodynamic equations must be recast and solved for a wind having an arbitrary direction.

The linearized hydrodynamic equations to be solved are

$$\frac{d\rho_1}{dt} + \rho_0 \underline{\nabla} \cdot \underline{v}_1 = 0, \tag{15a}$$

$$\rho_0 \frac{d}{dt}\underline{v}_1 = -\underline{\nabla} p_1 + \hat{e}_i \frac{\partial}{\partial x_j}\left[\eta\left(\frac{\partial v_{1i}}{\partial x_j} + \frac{\partial v_{1j}}{\partial x_i} - \frac{2}{3}\delta_{ij}\underline{\nabla} \cdot \underline{v}_1\right)\right], \tag{15b}$$

$$\frac{d}{dt}(p_1 - c_s^2 \rho_1) = (\gamma - 1)\alpha I, \tag{15c}$$

where ρ_1, $\underline{v}_1$, and p_1 represent the density, velocity, and pressure perturbations induced by laser heating, η is the viscosity, and the total derivative $\frac{d}{dt}$ is defined by

$$\frac{d}{dt} = \frac{\partial}{\partial t} + v_x \frac{\partial}{\partial x} + v_y \frac{\partial}{\partial y}. \quad (16)$$

Elimination of p_1 and v_1 yields the following equation for ρ_1:

$$\frac{d}{dt}\left(\frac{d^2}{dt^2}\ \rho_1 - c_s^2\nabla^2\rho_1 - \frac{4}{3}\frac{\eta}{\rho_0}\nabla^2\rho_1\right) = (\gamma - 1)\,\alpha\nabla^2 I\ . \quad (17)$$

We are interested in the steady state or the case in which Eq. (17) becomes

$$\left[\left(v_x \frac{\partial}{\partial x} + v_y \frac{\partial}{\partial y}\right)^2 - c_s^2\nabla^2 - \frac{4}{3}\frac{\eta}{\rho_0}\nabla^2\left(v_x \frac{\partial}{\partial x} + v_y \frac{\partial}{\partial y}\right)\right]\dot{\rho}_1 = (\gamma - 1)\alpha\nabla^2 I, \quad (18)$$

where

$$\dot{\rho}_1 = v_x \frac{\partial \rho_1}{\partial x} + v_y \frac{\partial \rho_1}{\partial y}\ . \quad (19)$$

The solution for ρ_1 is carried out in two steps: first Eq. (18) is solved with $\dot{\rho}_1$ as dependent variable, and then Eq. (19) is solved for ρ_1.

We shall restrict our attention to the subsonic case, where $v_x^2 + v_y^2 < c_s^2$. In that case Eq. (18) is elliptic and can be expressed in terms of a finite Fourier series representation:

$$\dot{\rho}_1(x,y) = \sum_{k_x,k_y} \tilde{\dot{\rho}}_1(k_x,k_y)\ \exp[i(k_x x + k_y y)]. \quad (20)$$

The coefficients $\dot{\rho}(k_x,k_y)$ satisfy

$$\tilde{\dot{\rho}}_1(k_x,k_y) = -\frac{(\gamma-1)}{c_s^2}\ \frac{\alpha\tilde{I}(k_x,k_y)(k_x^2 + k_y^2)}{\left\{(k_x^2 + k_y^2)\left[1 + \frac{4}{3}\,i\,\frac{\eta}{\rho_0 c_s^2}(v_x k_x + v_y k_y)\right] - \frac{(v_x k_x + v_y k_y)^2}{c_s^2}\right\}}\ , \quad (21)$$

where $\tilde{I}(k_x,k_y)$ is the Fourier transform of $I(x,y)$. The inverse Fourier transform of Eq. (21) is evaluated by means of the fast Fourier transform (FFT) algorithm. The function $\dot{\rho}_1(x,y)$ thus obtained then becomes

the source term for Eq. (19), which can be solved using the Carlson method[1] for integration along characteristics. The solution of Eq. (19) is obtained by a difference method in configuration space in preference to a Fourier transform method because the transform of $\rho_1(x,y)$ will have poles whenever $v_x k_x + v_y k_y = 0$. The evaluation of the inverse transform by the FFT algorithm will be troublesome, since these poles must be avoided.

If we define

$$\beta = \left| \frac{v_y \Delta_x}{v_x \Delta_y} \right| , \tag{22a}$$

$$i' = \frac{v_x}{|v_x|} , \tag{22b}$$

$$j' = \frac{v_y}{|v_y|} , \tag{22c}$$

the difference equation satisfied by $\rho_{ij} = \rho_1(i\Delta x, j\Delta y)$ can be written

$$\rho_{ij} = \frac{1}{\beta} \rho_{i-i',j-j'} + \left(1 - \frac{1}{\beta}\right) \rho_{i,j-j'} + \frac{\Delta_y}{2|v_y|} \left\{ \dot{\rho}_{i,j} + \frac{1}{\beta} \dot{\rho}_{i-i',j-j'} + \left(1 - \frac{1}{\beta}\right) \dot{\rho}_{i,j-j'} \right\} \text{ for } \beta > 1; \tag{23a}$$

$$\rho_{ij} = \beta \rho_{i-i',j-j'} + (1 - \beta) \rho_{i-i',j} + \frac{\Delta_y}{2|v_x|} \left\{ \dot{\rho}_{ij} + \beta \dot{\rho}_{i-i',j-j'} + (1 - \beta) \dot{\rho}_{i-i',j} \right\} \text{ for } \beta \leq 1. \tag{23b}$$

7. Steady-State Solutions of Hydrodynamic Equations for Arbitrary Transverse Wind Velocities: Multipulse Steady State

Isobaric density changes induced by multipulse heating are governed by the equation

$$\frac{\partial \rho_1^{mp}}{\partial t} + v_x \frac{\partial \rho_1^{mp}}{\partial x} + v_y \frac{\partial \rho_1^{mp}}{\partial y} = - \frac{\gamma - 1}{c_s^2} \alpha \sum_n \tau_p I_n(x,y) \, \delta(t - t_n) , \tag{24}$$

where $\tau_p I_n(x,y)$ represents the fluence of the nth pulse, and τ_p represents

the pulse width. If "steady-state" conditions prevail, it can be assumed that I_n does not vary from pulse to pulse. Hence $I_n(x,y) = I(x,y)$. Taking the Fourier transform of Eq. (24) with respect to x and y yields

$$\frac{\partial \tilde{\rho}_1^{mp}}{\partial t} + i(v_x k_x + v_y k_y)\tilde{\rho}_1^{mp} = -\frac{\gamma - 1}{c_s^2}\ \alpha \tau_p \tilde{I}(k_x,k_y)\ \sum_n \delta(t - t_n). \qquad (25)$$

Solving Eq. (25) for $\tilde{\rho}_1^{mp}$ at a time $t = m\Delta t$, where m is any integer and Δt is the time interval between successive pulses, gives

$$\tilde{\rho}_1(k_x,k_y,m\Delta t) = -\frac{\gamma - 1}{c_s^2}\ \alpha\ \tilde{I}(k_x,k_y) \sum_{n=1}^{N_p} \exp[-in\Delta t(k_x v_x + k_y v_y)]. \qquad (26)$$

The exponentials in Eq. (26) correspond to translations of the individual-pulse fluence distributions in configuration space by wind motion.

The summation begins with $n = 1$ because the isobaric density changes created by a given pulse do not have time to develop during the pulse width, τ_p. The upper limit N_p is based on numerical considerations and is determined by

$$N_p = \text{MIN}\left(N_{\text{input}}, \left[\frac{N\Delta x}{|v_x|\Delta t}\right], \left[\frac{N\Delta y}{|v_y|\Delta t}\right]\right), \qquad (27)$$

where N is the numerical length of the mesh used for solving the wave equation.

In Eq. (27) MIN signifies the minimum of the arguments, and the square brackets represent the integer part of the arguments inside them. An input value of N_p is useful if a true stagnation point is encountered along the propagation path. In such cases the total density change at the stagnation point can be kept bounded. For example, N_{input} might be set equal to the actual number of pulses in a given train, in which case a true lower bound could be assigned to the intensities at the target.

The remaining arguments in Eq. (27) prevent any pulse fluence distribution from affecting the density calculation if it has been translated by more than the minimum (physical) dimension of the computational mesh for the wave equation, i.e. $\text{MIN}(N\Delta x, N\Delta y)$.

The density calculation itself is carried out on a $2N \times 2N$ mesh, which has a buffer of length N in both the x and y directions. Thus if N_p satisfies condition (27), periodic "wrap-around" or positional aliasing of the density contributions by past pulses in the train is avoided.

The summation in Eq. (26) may be evaluated directly, and $\tilde{\rho}_1$ can be expressed in the form

$$\tilde{\rho}_1(k_x,k_y) = -\frac{\gamma - i}{\sigma_s^2}\,\alpha\tilde{I}(k_x,k_y)\,\exp\left[-i\frac{N_p+1}{2}\,\Delta t(k_x v_x + k_y v_y)\right] \times \frac{\sin\frac{N_p}{2}\Delta t(k_x v_x + k_y v_y)}{\sin\frac{\Delta t}{2}\,(k_x v_x + k_y v_y)} \quad . \qquad (28)$$

The density $\rho_1(x,y)$ is then obtainable from Eq. (28) by an inverse transform operation using the FFT algorithm. Equation (28) has been used in a number of test examples with satisfactory results. If the spectrum $I(k_x,k_y)$ is particularly rich in high spatial frequencies, Eq. (28) may give rise to a ringing behavior in configuration space due to the fact that the shift operators

$$\exp(-in\Delta t k_x v_x),\ \exp(-in\Delta t k_y v_y) \qquad (29)$$

may not correspond to lattice translation operators on the computational mesh. In such a case ringing can be suppressed by expressing the solution of Eq. (26) in terms of the interpolations of lattice shift operations.

By means of bilinear interpolation, one can express any function $T(x,y)$ at positions intermediate to the lattice by means of

$$T_{j+f_x,k+f_y} = (1-f_y)\,f_x\,T_{j+1,k} + (1-f_x)\,f_y\,T_{j,k+1} + f_x f_y\,T_{j+1,k+1} + (1-f_y)(1-f_x)\,T_{j,k}\ , \qquad (30)$$

$$0 < f_x \leq 1\ ,\ 0 < f_y \leq 1\ ,$$

where f_x and f_y represent fractional distances between lattice coordinates, and where the numbers $T_{j,k}$ represent values of $T(x,y)$ sampled at lattice points. The summation in Eq. (26) may thus be represented in the following alternative form, which avoids the use of nonlattice shift operators (the notation [ ] signifies the integer part of the argument):

$$\sum_{n=1}^{N_p} \exp\{-in\Delta t(k_x v_x + k_y v_y)\}$$

$$= \sum_{n=1}^{N_p} \left\{ f_x(1-f_y) \exp\left(i \frac{\pi}{N}\left\{n_{k_x}([\eta_x n]+1) + n_{k_y}[\eta_y n]\right\}\right)\right.$$

$$+ f_y(1-f_y) \exp\left(i \frac{\pi}{N}\left\{n_{k_x}[\eta_x n] + n_{k_y}([\eta_y n]+1)\right\}\right)$$

$$+ f_x f_y \exp\left(i \frac{\pi}{N}\left\{n_{k_x}([\eta_x n]+1) + n_{k_y}([\eta_y n]+1)\right\}\right)$$

$$\left. + (1-f_y)(1-f_x) \exp\left(i \frac{\pi}{N}\left\{n_{k_x}[\eta_x n] + n_{k_y}[\eta_y n]\right\}\right)\right\} = g(k_x, k_y), \qquad (31)$$

where

$$\left.\begin{aligned} \eta_x &= \frac{v_x \Delta t}{\Delta x}, \\ \eta_y &= \frac{v_y \Delta t}{\Delta y}, \\ f_x(n) &= \eta_x n - [\eta_x n], \\ f_y(n) &= \eta_y n - [\eta_y n]. \end{aligned}\right\} \qquad (32)$$

The summation in Eq. (26) over n can be evaluated as a $2N \times 2N$ DFT with the aid of the FFT algorithm. For a given value of n, the numbers $[\eta_x n]$, $[\eta_x n] + 1$ can each be identified as x-coordinates n_x and the numbers $[\eta_y n]$, $[\eta_y n] + 1$ as y-coordinates n_y in the lattice space. Thus each exponential in the summation in Eq. (31) can be identified with a particular lattice point n_x, n_y. As the index n is incremented, the appropriate bilinear function of $f_x(n)$ and

$f_y(n)$ is added to the contents of a storage register corresponding to coordinates n_x, n_y. On completion of this operation, a two-dimensional DFT of the resultant array will yield the desired sum (31).

The Fourier transform of the density can then be expressed as

$$\tilde{\rho}_1(k_x,k_y,m\Delta t) = -\frac{(\gamma - 1)}{\sigma_s^2} \times \alpha\tilde{I}(k_x,k_y)\,\tilde{g}(k_x,k_y) \ . \qquad (33)$$

Both the options (28) and (29) are currently available in the Four-D code, and the cases run have produced results that are almost indistinguishable.

The shifts and interpolations implied in Eq. (31) may, of course, be carried out strictly in configuration space. If N_p is small, this procedure may be more economical. As N_p becomes large, the Fourier transform method becomes more economical.

8. Effect of Noncoplanarity on Propagation of cw Laser Beams Through Stagnation Zones

We shall focus attention on the scenario discussed in Ref. 1, in which the total propagation distance is 1.5 km and the stagnation point occurs at $z = 0.8439$ km. The initial diffraction-limited beam is Gaussian, with $1/e^2$-intensity diameter of 70 cm, and is assumed to be focused at the 1.5-km range. The wavelength and absorption coefficient are assumed to be 3.8 μm and 0.07 km^{-1}, respectively. For reference the results of the time dependent calculations at $t = 60$ ms are given in Table 5. For this value of t, the beam properties are changing very slowly, and the assumption of a "quasi" steady state is a reasonable one.

In the noncoplanar scenario, on the other hand, a true steady state is known to exist, and a time to establish this steady state can be estimated by dividing the beam diameter by the magnitude of the vertical wind component at the stagnation point. The noncoplanar results are naturally much cheaper to obtain than the corresponding coplanar results.

In Table 6, steady-state results are given for the scenario corresponding to Table 5 for a variety of elevations of the laser aperture

Table 5. Beam properties on target at t = 60 ms.

Laser power (kW)	Peak intensity at target (kW/cm^2)	Minimum half-power area (cm^2)	Intensity averaged over minimum half-power area (kW/cm^2)
500	10.8	33.4	6.72
500[a]	9.8	53.5	4.19
500[b]	11.0	33.2	6.76
250	12.4	13.5	8.34
125	17.7	4.42	12.7
62.5	22.7	1.65	17.0

[a]Focus 100 m beyond range.

[b]Motion of stagnation zone taken into account.

Table 6. Steady-state cw beam properties as a function of laser height above scenario plane.

Laser power (kW)	Laser elevation (m)	Vertical wind speed at stagnation point (m/s)	Minimum half-power area (stagnation point) (cm^2)	Minimum half-power area (target) (cm^2)	Time to steady state (s)	Peak intensity at target (kW/cm^2)	Intensity averaged over minimum half-power area at target (kW/cm^2)
500	5	0.55	293	37.7	0.312	11.0	5.97
	10	1.1	291	33.6	.155	12.0	6.69
	20	2.2	290	29.1	.077	14.0	7.72
	30	3.3	289	26.4	.052	15.9	8.52
	40	4.4	287	23.6	.039	16.1	9.53
250	5	0.55	279	13.7	.303	16.6	8.2
	10	1.1	278	12.0	.152	17.8	9.36
	20	2.2	277	10.1	.076	19.5	11.0
	30	3.3	278	8.9	.051	21.6	12.6
	40	4.4	276	7.88	.038	24.1	14.3
125	5	0.55	272	4.66	.300	22.9	12.0
	10	1.1	271	4.04	.150	25.3	13.9
	20	2.2	271	3.33	.075	28.6	19.5
	40	4.4	270	2.31	.037	39.7	24.3
62.5	5	0.55	268	1.58	.29	30.6	17.7
	10	1.1	268	1.37	0.14	34.3	20.5

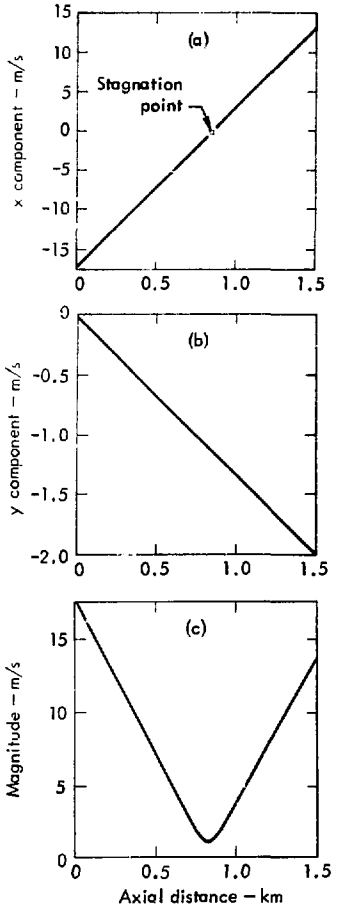

Fig. 12. Transverse wind velocity as a function of axial distance for cw beam. (a) x component. (b) y component. (c) Magnitude.

above the scenario plane. Figure 12 shows the variations with z of the horizontal and vertical components and the magnitude of the transverse wind.

From Tables 5 and 6, it is evident that the space-averaged intensities in the focal plane for the noncoplanar scenario at 5-m elevation agree with the corresponding average steady-state intensities for

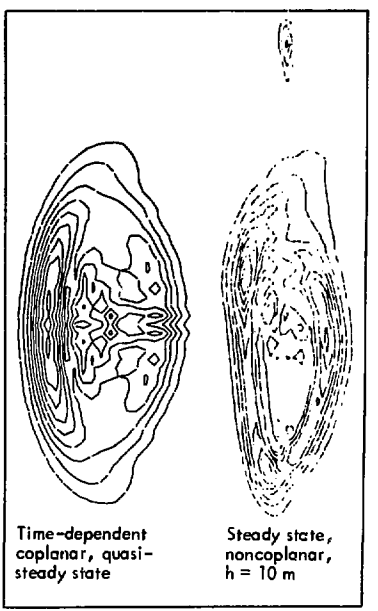

Fig. 13. Comparison of isointensity contours for stagnation-zone situations in coplanar and noncoplanar cases.

the coplanar scenarios to within less than 10%. The peak intensities for the noncoplanar scenario at 5 m, on the other hand, are somewhat higher than the corresponding values for the coplanar case. There is also a substantial difference in the appearance of the isointensity contours in the focal plane (Fig. 13). As would be expected, performance improves with height, although the improvement is marginal for the elevations considered. In all cases a steady-state condition can be reached in a time small compared with times of interest.

In conclusion, average intensities for coplanar stagnation-zone scenarios can be calculated by adding nominal noncoplanar features to the scenario and performing a steady-state calculation. For ;w beams, however, rather substantial laser elevations must be provided to alleviate stagnation-zone effects.

9. Effect of Noncoplanarity of Propagation of Multipulse Beams Through Stagnation Zones

We turn our attention again to the scenario of Section 3. All problem parameters are the same, except that the laser is now assumed to be elevated 10 m above the scenario plane. Figure 14 shows the vertical and horizontal components of transverse wind velocity as functions of propagation distance. Figure 15 shows the isointensity contours in the target plane for the various repetition rates.

Table 7 compares laser performance on target as a function of pulse-repetition frequency for the coplanar scenario and the noncoplanar scenario with a laser elevation of 10 m. In the absence of complete steady-state data for the coplanar case, we have used in Table 7 intensity values corresponding to the final times exhibited in Fig. 6 for a given value of ν. Thus the improvements due to noncoplanarity shown in Table 7 are conservative estimates.

It is seen from Table 7 that improvements of at least a factor of 2, conservatively estimated, are possible for all values of ν. In the case of $\nu = 10\ s^{-1}$ the laser performance is even better than it would be in a vacuum. The reason is that for this pulse-repetition frequency the overlap number at the stagnation point is only 2, and for

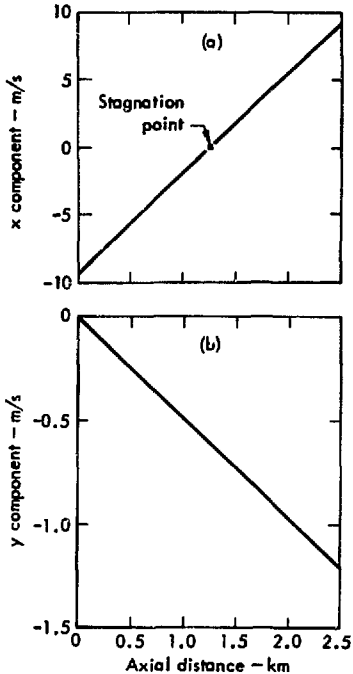

Fig. 14. Transverse wind velocity as a function of axial distance for multipulse beam. (a) x component. (b) y component.

overlap numbers in the range 1-2 such enhancement effects for multipulse beams are well known.[6]

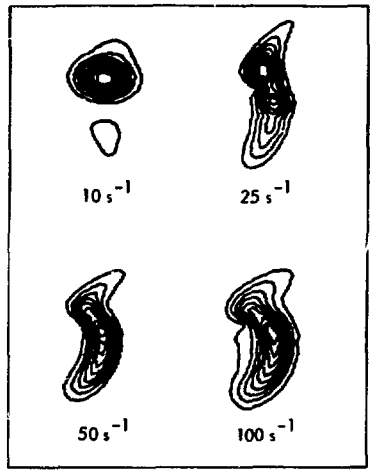

Fig. 15. Changing shapes of isointensity contours as a function of pulse-repetition rate for noncoplanar scenario; laser at 10-m elevation.

To summarize: there is clearly some hope of minimizing stagnation-zone blooming for multipulse beams by a combination of elevating the laser aperture above the scenario plane and lowering the pulse-repetition frequency.

Table 7. Comparison of multipluse beam properties for coplanar and non-coplanar scenarios. Power = 53 kW, range = 2.5 km, λ = 10.6 μm, elevation h = 10 m, and vertical wind speed at stagnation point = 0.61 m/s.

Pulse repetition frequency, ν (s^{-1})	Minimum half-power area (stagnation point, noncoplanar scenario) (cm^{-2})	Time to steady state (non-coplanar scenario) (s)	Overlap number at stagnation point (non-coplanar scenario)	Peak intensity at target (coplanar scenario) (W/cm^2)	Peak intensity at target (non-coplanar scenario) (W/cm^2)	Intensity averaged over minimum half-power area (coplanar scenario) (W/cm^2)	Intensity averaged over minimum half-power area (non-coplanar scenario) (W/cm^2)
10	131	0.19	1.9	85.5[c]	287[a]	52.0[c]	181[b]
25	116	0.18	4.49	79.5[c]	116	32.5[c]	65.6
50	104	0.17	8.49	28.7[d]	70.9	17.8[d]	42.3
100	140	0.19	19.0	30.4[d]	49.0	13.2[e]	30.3

[a] Vacuum beam has value 238.

[b] Vacuum beam has value 170.

[c] t = 0.6 s, steady state has not been reached.

[d] t = 0.32 s, steady state has not been reached.

[e] t = 0.2 s, steady state has not been reached.

10. Single-Pulse Thermal Blooming in the Triangular Pulse Approximation

The isobaric approximation for changes in air density is invalid for a single laser pulse whose duration is comparable to or less than the transit time of sound across the beam. In this time regime — referred to as the t^3-regime because of the time dependence of density changes arising from an applied constant laser-energy absorption rate — the air-density changes must be determined from the complete set of time-dependent hydrodynamic equations, Eqs. (15).[1,7]

At late times in the pulse, t^3 thermal blooming tends to reduce the on-axis intensity relative to what it would be if the beam were propagating in vacuum. This reduction increases with time, and for sufficiently late times a depression appears in the center of the beam. Energy added to the pulse at later times will contribute only marginally to the on-axis fluence. Thus, for a specific peak pulse intensity, the on-axis fluence appears to saturate as the pulse

duration is stretched out more and more.

These properties are best illustrated by a numerical example. Let us consider a beam that is Gaussian at $z = 0$ with $1/e^2$-intensity radius 25 cm. The beam, which is focused at 2.5 km, is assumed to be 2× diffraction limited (λ-scaled) with $\lambda = 10.59$ μm and $\alpha = 0.3 \times 10^{-5}$ cm^{-1}. The pulse is square-shaped in time and lasts 100 μs. The choice of a square-shaped pulse is convenient because a single calculation contains the complete information for all square pulses of duration shorter than the one chosen.

Figure 16 shows the on-axis intensity at $z = 2.0$ km, obtained by detailed numerical solution[1] of Eqs. (15). The on-axis intensity clearly drops to a negligible value before the end of the pulse, and, as a consequence, the on-axis fluence saturates as the pulse width increases, as can be seen in Fig. 17. The detailed temporal evolution of the spatial shape of the beam is shown in Figs. 18 and 19. Figure 18 is a three-dimensional plot of the laser intensity as a function of time and radius. Figure 19 shows the radial intensity profiles for increasing values of time. The opening up of a hole in the back of the pulse is clear from both Figs. 18 and 19.

Calculations of the type represented in Figs. 17-19 become impractical if one is treating a

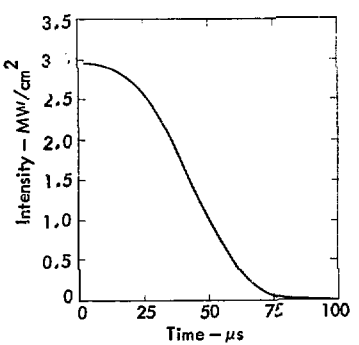

Fig. 16. On-axis intensity as a function of time. The pulse is taken to be square-shaped in time. Thermal blooming reduces on-axis intensity to a negligible value after a sufficiently long time.

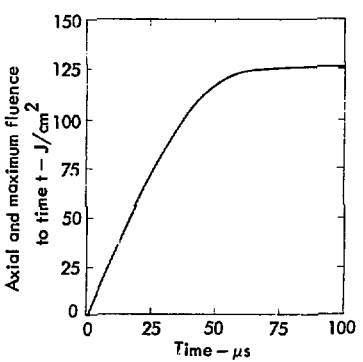

Fig. 17. Saturation of on-axis fluence due to strong pulse thermal blooming.

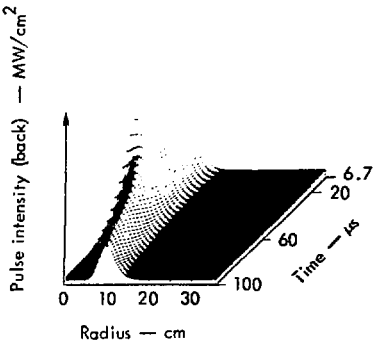

Fig. 18. Three-dimensional plot of intensity as a function of time and radius corresponding to Figs. 16 and 17.

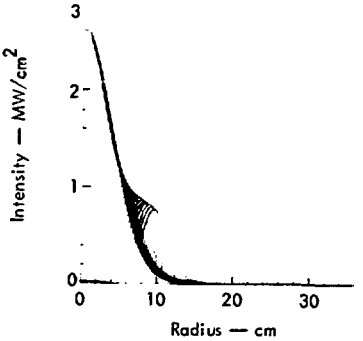

Fig. 19. Intensity as a function of radius for increasing time in pulse corresponding to Figs. 16 and 17.

multipulse beam. The determination of nonisobaric contributions to the density is greatly simplified by the triangular pulse approximation,[1] in which the dependence of the laser intensity on time is represented as an isosceles triangle with base equal to $2\tau_p$. The density is required only at time $t = \tau_p$, since the laser intensity is assumed to vanish for $t = 0$ and $t \geq 2\tau_p$.

The density change at $t = \tau_p$ can be evaluated analytically in terms of a finite Fourier series representation of the laser intensity. The Fourier transform of the nonisobarically induced density change is

$$\tilde{\rho}_1^{sp} = -(\gamma - 1)\frac{\alpha\tilde{I}\tau_p}{2c_e^2}\left\{1 - \frac{\sin^2\left[\frac{1}{2}c_s\tau_p\left(k_x^2 + k_y^2\right)^{1/2}\right]}{\left[\frac{1}{2}c_s\tau_p\left(k_x^2 + k_y^2\right)^{1/2}\right]^2}\right\}, \tag{34}$$

where $\tilde{I}$ is the spatial Fourier transform of the intensity. The corresponding density changes at the grid points are given by the discrete Fourier transform (DFT) expression

$$\rho_1^{sp}(j\Delta x, k\Delta y) = (2N)^{-2}\sum_{m,n=-N+1}^{N}\tilde{\rho}_1^{sp}\left(\frac{\pi m}{L}, \frac{\pi n}{L}\right)\exp\left(2\pi i\frac{mj + nk}{2N}\right), \tag{35}$$

where the basis functions are periodic on a square of side $2L$. This allows for a buffer region that extends an additional distance L in both the x and y directions from the region of interest.

Comparison of the triangular pulse approximation and detailed pulse thermal-blooming calculations for Gaussian-shaped pulses in time have shown good agreement between the calculated fluences for weak or moderate thermal blooming.[1]

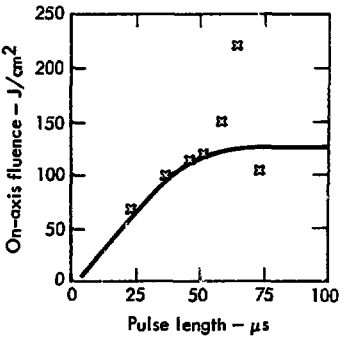

Fig. 20. On-axis fluence as a function of pulse length, as calculated with triangular pulse approximation (x's) and by detailed numerical solution of hydrodynamic equations for a square pulse in time (solid curve). The triangular pulse approximation breaks down as saturated-fluence condition sets in at $\tau_p \approx 1.5t_s$. Erratic behavior is due to development of spikes in the intensity pattern as a function of transverse position.

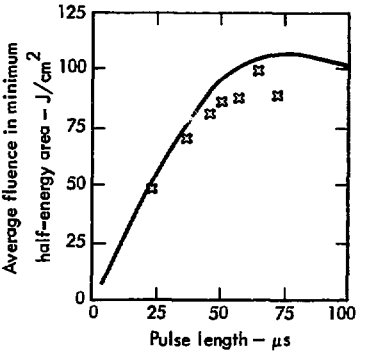

Fig. 21. Fluence averaged over minimum area containing one half of total beam energy, as a function of pulse length. Solid curve is detailed calculation for square pulse, x's represent triangular pulse approximation.

Figure 20 shows the on-axis fluence calculated for the previous example with the triangular pulse approximation (x's) and the detailed solution of Eqs. (15) for square pulses in time (solid line). Despite the difference in assumed pulse shapes, the agreement between the two types of calculation is very good up until time $t \approx 50$ μs, which is well above the saturation time $t_s = 38$ μs predicted by the perturbation theory of Ulrich and Hayes[8] based on the work of Aitken *et al.*[9] Above 55 μs, or approximately $1.5t_s$, the beam abruptly develops spikes in its transverse spatial dependence;

this clearly signals the breakdown of the triangular pulse approximation, which must obviously fail when strong saturation behavior sets in.

Figure 21 shows the fluence averaged over the minimum half-energy area (the area within the one-half peak energy contour) calculated with the triangular pulse approximation and with the detailed solution of Eqs. (15) for square pulses. Both calculations increase initially, reach a maximum, and then turn over with increasing time. This is in part due to the increase of the area within the one-half peak energy contour with time. There is, however, no point in believing the triangular pulse approximation beyond the time when the average fluence curve has reached a maximum, which also coincides with the onset of erratic behavior in the on-axis fluence (Fig. 20).

The perturbation theory alluded to earlier[8,9] describes the on-axis fluence saturation for a beam that is initially Gaussian in shape and for a pulse shape that is square in time. In this theory, the expression for the on-axis intensity is

$$I(t) = \begin{cases} I_0(z)\left(1 - \dfrac{t^3}{t_s^3}\right) & t \le t_s \\ 0 & t > t_s, \end{cases} \qquad (36)$$

where $I_0(z)$ is the on-axis intensity for a Gaussian beam propagating in vacuum, or

$$I_0(z) = \frac{I_0(0)\, e^{-\alpha z}}{D(z)} . \qquad (37)$$

Here α is the absorption coefficient and

$$D(z) = \left(1 - \frac{z}{f}\right)^2 + \left(\frac{z}{ka^2}\right)^2 , \qquad (38)$$

where f is the focal distance and a is the radius of the original Gaussian beam. The saturation time t_s at on-axial position z is given by

$$t_s = \left[\frac{2N(\gamma - 1)\, \alpha z^2 E_p e^{-\alpha z}}{3\pi a^6 D^2(z)\, \tau}\right]^{-1/3} \qquad (39)$$

where N is the refractivity, E_p is the pulse energy, and τ_p is the pulse duration. Since the fluence cannot be increased for pulses longer than t_s, it can be argued that nothing is accomplished by making the pulse longer than t_s. The fluence must be maximized instead by maximizing the product $I_0(z)\, t_s$ or, equivalently, by maximizing $I_0(z)$. The maximum allowable value of $I_0(z)$ at point z is normally determined by the condition that it not exceed the breakdown intensity, or

$$\max I_0(z) = I_{BD} \quad . \tag{40}$$

This maximum allowable intensity in turn determines a critical input pulse energy at $z = 0$ given by

$$E_{crit} = \pi a^2 t_s I_{BD} D(z) e^{\alpha z} \quad , \tag{41}$$

where Eq. (37) has been made use of, and where t_s is calculated from

$$t_s = \left[\frac{2N(\gamma - 1)\, \alpha z^2 I_{BD}}{3a^4 D(z)} \right]^{-1/3} \quad . \tag{42}$$

If one is dealing with a multipulse laser with pulse-repetition frequency ν, Eq. (41) can be used to define a critical input power with

$$P_{crit} = \nu E_{crit} = \pi a^2 \nu t_s I_{BD} D(z) e^{\alpha z} \quad . \tag{43}$$

The self-consistency of the triangular pulse approximation, on the other hand, prevents the on-axis intensity from ever becoming negative, but, as previously remarked, the triangular pulse approximation breaks down for pulse energies greater than the value that maximizes the space-averaged target fluence. For this pulse energy, the average and on-axis fluences should be saturated, and further increases in pulse energy would give no return. Figures 22 and 23 have been calculated with the data on which

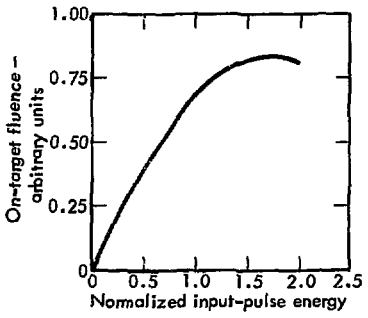

Fig. 22. On-target fluence from triangular pulse approximation averaged over area containing $(1 - 1/e)$ fraction of total beam energy. Range ≈ 1.5 km, $I_{BD} = 1.6 \times 10^6$ W/cm^2.

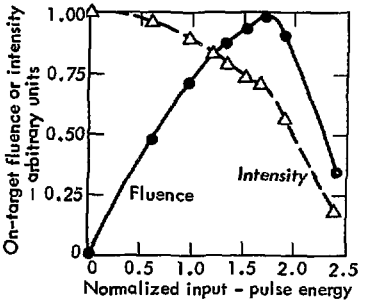

Fig. 23. On-target space-averaged fluence and intensity as functions of input pulse energy for triangular pulse approximation. Range = 2 km, $I_{BD} = 3 \times 10^6$ W/cm^2.

Figs. 16-21 are based, but with the following differences: the ranges for Figs. 22 and 23 are 1.5 km and 2.0 km respectively; the values assigned (somewhat arbitrarily) to I_{RD} at these ranges are 3×10^6 W/cm^2 and 1.5×10^6 W/cm^2.

Both the on-target space-averaged fluence and intensity (Fig. 23) are plotted as functions of the input pulse energy normalized to E_{crit} given in Eq. (42). The space averaging is over the area contained within the $1/e$ energy contour. The indicated maxima of the average fluences in both Figs. 22 and 23 occur at an input pulse energy equal to $1.7E_{crit}$. The space-averaged fluence curves in Figs. 22 and 23 are smoother than those displayed in Fig. 20 because the former are averaged over larger areas. The scaling implications of the perturbation theory described in Eqs. (36)-(42) are apparently valid for the triangular pulse approximation, although the maximum useful pulse energy predicted by the latter is about 50% greater than that predicted by the perturbation theory.

In summary: the triangular pulse approximation should provide reasonably accurate fluence results for pulse energies up to the values where strong thermal blooming saturates the on-axis fluence. The breakdown of the approximation will be indicated by the development of spikes in the transverse spatial dependence of the beam intensity as well as by a sharp falloff in the fluence averaged over some area as a function of pulse energy.

11. Multipulse Thermal Blooming in the Triangular Pulse Approximation

The propagation of a given pulse in a train is influenced by both the nonisobaric density changes discussed in the previous section and by the isobaric density changes due to heating by previous pulses in the train. But can the self-blooming and multipulse blooming effects be treated independently? If so, the results and discussion of the previous section suggest that, as time-averaged laser power is increased by lengthening the duration of the constituent pulses in the train, the time-averaged intensity on target should saturate at a value that is predictable from the saturation fluence for a single

pulse. If $\langle I \rangle$ represents the time-averaged intensity, the maximum achievable value of $\langle I \rangle$ for a given pulse-repetition rate should be expressible as

$$\langle I \rangle_{max} = \nu F_{sat} , \qquad (44)$$

where F_{sat} is the single-pulse saturation fluence.

In order to test the hypothesis of the independence of self and multipulse blooming, a set of calculations has been carried out with the following set of parameters:

Start beam shape	Gaussian, truncated at $1/e^2$ radius
Range, R	2.5 km
Focal length/range, F/R	1.0 and 1.2
Wavelength, λ	10.6 μm
Absorption coefficient, α	0.25 km^{-1}
Aperture diameter, $2a$ (Gaussian at $1/e^2$)	21.2 cm
Wind velocity, v_0	10 m/s
Pulse-repetition rate, ν	33-1/3 and 50 s^{-1}
Maximum pulse intensity at receiver, I_{max}	4.9 MW/cm^2
Overlap number, $N_0 = 2a\nu/v_0$	1.0, 1.5

Figure 24 shows the space-averaged single-pulse intensity $\bar{I}$ for ν = 33-1/3 s^{-1} and N_0 = 1, with F/R = 1.0 and 1.2, calculated as a function of input time-averaged power $\langle P \rangle = \nu E_p$. The curves have been calculated with and without the effects of pulse self-blooming. The curve without self-blooming for F/R = 1.2 rises slightly with input power because of a very slight amount of pulse overlap. It is clear from Fig. 24, in any case, that thermal blooming is due almost entirely to self-blooming effects. The corresponding curves for space- and time-averaged target intensities $\langle \bar{I} \rangle$ are displayed in Fig. 25, where

$$\langle \bar{I} \rangle = \bar{I}\tau\nu . \qquad (44)$$

It is seen that $\langle \bar{I} \rangle$ with self-blooming rises initially, reaches a peak, and then falls. From the analysis of the previous section, we interpret the peak values of $\langle \bar{I} \rangle$ as the saturated values.

Figure 26 shows $\bar{I}$ as a function of $\langle P \rangle$ for ν = 50 s^{-1} and N_0 = 1.5, with F/R = 1.0 and 1.2. Above $\langle P \rangle$ = = 0.5 MW, and an enhancement effect sets in that is greater in the case of the defocused beam. The corresponding curves for space- and time-averaged target intensities are shown in Fig. 27.

A comparison of Figs. 25 and 27 is summarized in Table 8. It is seen that at ν = 50 s^{-1} the power $\langle P \rangle_{sat}$ at which saturation of $\langle \bar{I} \rangle$ occurs is

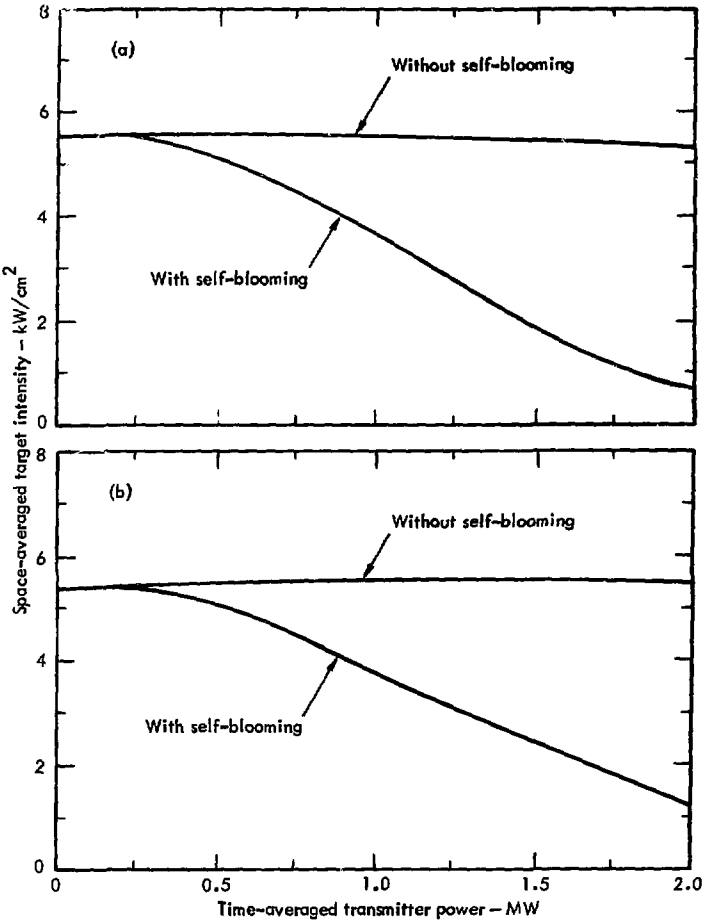

Fig. 24. Space-averaged intensity on target as a function of time-averaged power at transmitter: ν = 33-1/3 s^{-1}, N_0 = 1. (a) F/R = 1.0. (b) F/R = 1.2.

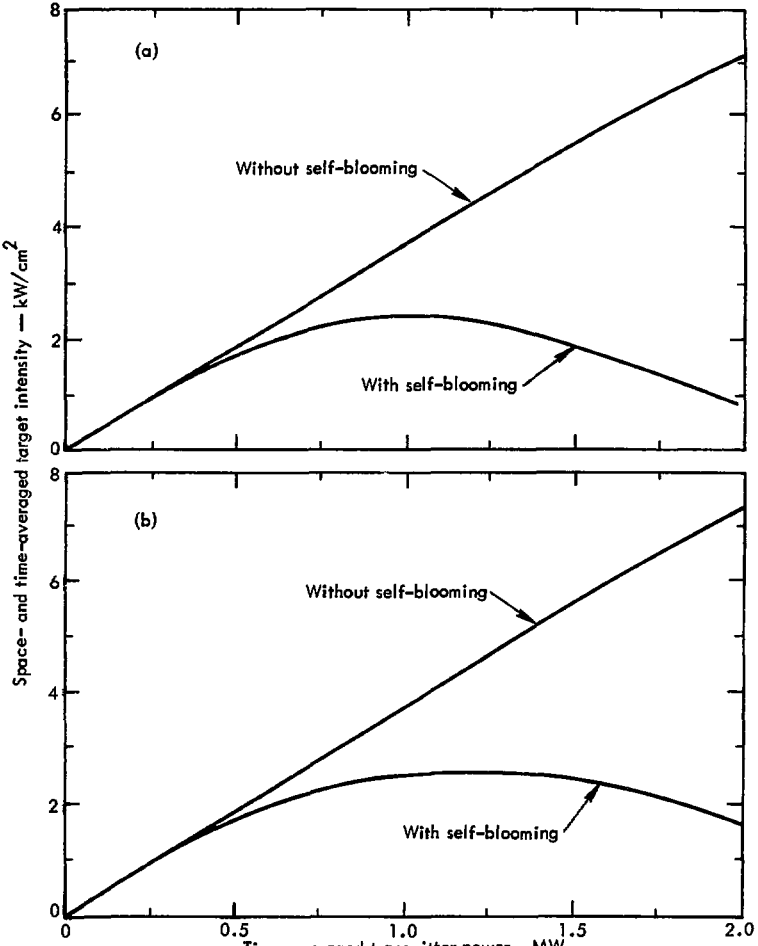

Fig. 25. Space- and time-averaged intensity on target as a function of time-averaged power at transmitter: ν = 33-1/3 s^{-1}, N_0 = 1. (a) F/R = 1.0. (b) F/R = 1.2.

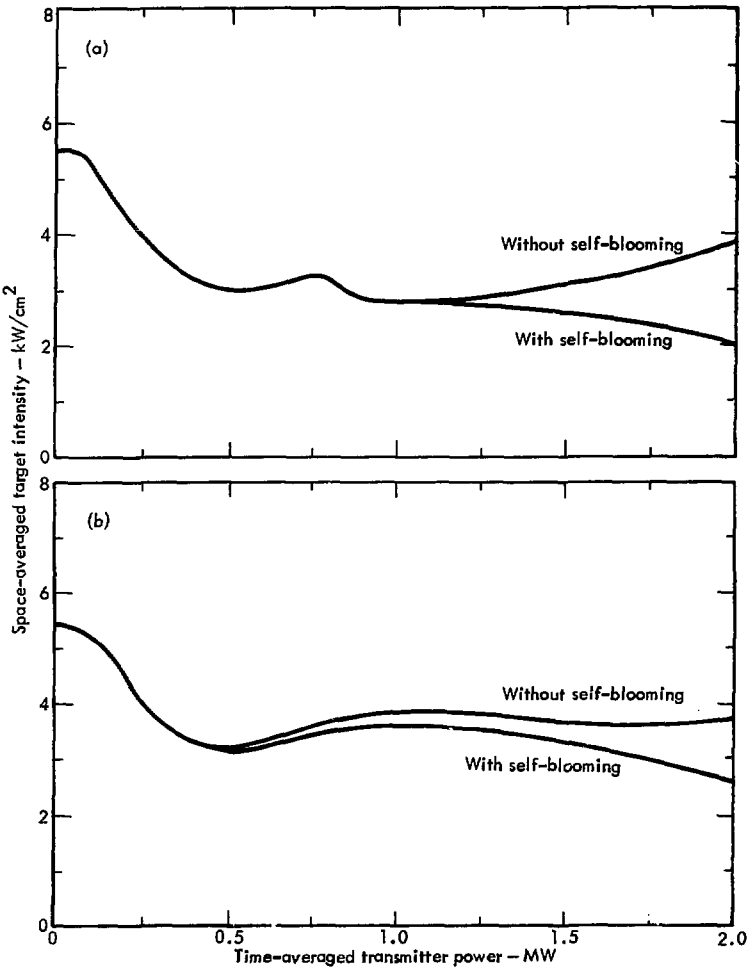

Fig. 26. Space-averaged intensity on target as a function of time-averaged power at transmitter: $\nu = 50\ s^{-1}$, $N_0 = 1.5$. (a) $F/R = 1.0$. (b) $F/R = 1.2$.

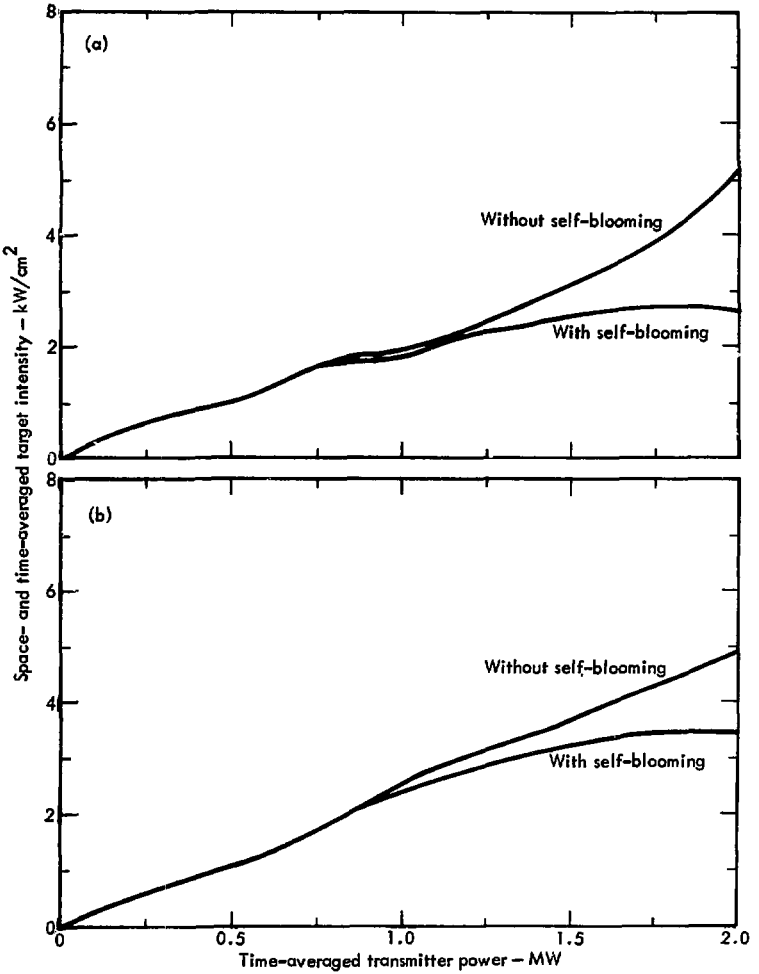

Fig. 27. Space- and time-averaged intensity on target as a function of time-averaged power at transmitter: $\nu = 50\ s^{-1}$, $N_0 = 1.5$. (a) $F/R = 1.0$. (b) $F/R = 1.2$.

Table 8. Saturation of time- and space-averaged target intensity due to self-blooming.

ν (s^{-1})	F/R	$\langle P \rangle_{sat}$ (MW)	$\langle \bar{I} \rangle_{sat}$ (kW/cm^2)
33 1/3	1.0	1.0	2.4
33 1/3	1.2	1.2	2.5
50	1.0	1.75	2.7
50	1.2	2.0	3.5

higher for both values of F/R than it is at ν = 33-1/3 s^{-1}. The corresponding saturation intensity values $\langle I \rangle_{sat}$ are also greater at ν = 50 s^{-1} than at ν = 33-1/3 s^{-1}. If effects of self-blooming are not included, on the other hand, values of $\langle \bar{I} \rangle$ are always greater at a given value of $\langle P \rangle$ in the case of ν = 33-1/3 s^{-1}.

Unfortunately, we have no guide to the accuracy of the triangular pulse approximation in the overlap case as we do in the nonoverlap case. But the above results strongly suggest that the contributions of isobaric and nonisobaric density changes to thermal blooming of multipulse beams are interrelated, and that time-averaged saturation intensities based on single saturation fluences may not be applicable for overlap numbers somewhat above 1. In fact, overlapping isobaric density patterns may in certain situations actually override the effects of single-pulse nonisobaric density changes.

Acknowledgment

The authors are indebted to C. H. Woods for the calculations of the effects of laser elevation on cw laser performance in Section 9 and for the effects of pulse thermal blooming on multipulse propagation in Section 11.

References

1. J. A. Fleck, Jr., J. R. Morris, and M. Feit, *Time-Dependent Propagation of High Energy Laser Beams Through the Atmosphere*, Lawrence Livermore Laboratory, Rept. UCRL-51826 (1975); UCRL-77719 (1976) to be published in *Applied Physics*.
2. R. T. Brown, P. J. Berger, F. G. Gebhardt, and H. C. Smith, *Influence of Dead Zones and Transonic Slewing on Thermal Blooming*, United Aircraft Research Laboratory, East Hartford, Conn., Rept. N921724-7 (1974).
3. P. J. Berger, F. G. Gebhardt, and D. C. Smith, *Thermal Blooming Due to a Stagnation Zone in a Slewed Beam*, United Aircraft Research Laboratory, East Hartford, Conn., Rept. N921724-12 (1974).
4. P. J. Berger, P. B. Ulrich, J. T. Ulrich, and F. G. Gebhardt, "Transient Thermal Blooming of a Slewed Laser Beam Containing a Regime of Stagnant Absorber," submitted to *Applied Optics*.
5. The possibility of such curved flow trajectories in the neighborhood of the stagnation point was pointed out to one of the authors by B. Hogge, private communication.
6. J. Wallace and J. R. Lilly, "Thermal Blooming of Repetitively Pulsed Laser Beams," *J. Opt. Soc. Am.* 64, 1651 (1974).
7. P. B. Ulrich and J. Wallace, *J. Opt. Soc. Am.* 63, 8 (1973).
8. P. B. Ulrich and J. N. Hayes, U.S. Naval Research Laboratory, Washington, D.C., unpublished internal report (1974).
9. A. H. Aitken, J. N. Hayes, and P. B. Ulrich, "Thermal Blooming of Pulsed Focused Gaussian Laser Beams," *Appl. Opt.* 12, 193 (1973).

Appendix A: Adaptive Lens Transformation

One key to the successful implementation of a laser-propagation code is finding a coordinate transformation that keeps the laser beam away from the calculational mesh boundary and at the same time prevents the beam from contracting to an unreasonably small fraction of the total mesh area at the focus. If one is solving the Fresnel equation by the finite Fourier transform method, one may alternatively view the problem in terms of complementarity: one wishes to find a transformation that simultaneously keeps the beam intensity small on the mesh boundaries in configuration space and keeps the Fourier spectrum small on the mesh boundaries in k-space. If these two conditions are met, one knows from sampling theory that the numerical solution is highly accurate.

The Four-D code uses an automated procedure that is designed to keep the intensity centroid at the center of the mesh and the intensity-weighted r.m.s. values of x and y constant with propagation distance z. These conditions can be written

$$\frac{\partial}{\partial z} \langle x_i \rangle = 0, \tag{A1a}$$

$$\frac{\partial}{\partial z} \langle (x_i - \langle x_i \rangle)^2 \rangle = 0 , \qquad i = 1, 2 , \tag{A1b}$$

$$x_1 = x, \; x_2 = y ,$$

where

$$\langle u \rangle = \frac{\int dx \; dy \; I(x,y) u}{\int dx \; dy \; I(x,y)} . \tag{A1c}$$

Hereafter, all averages will be assumed to be intensity-weighted, and the subscript I will be dropped.

Conditions (A1) also apply to the adaptive coordinate transformation of Bradley and Hermann,[A1] which differs from the one employed in the Four-D

A1. L. C. Bradley and J. Hermann, "Change of Reference Wavefront," Massachusetts Institute of Technology, Lincoln Laboratory, Lexington, Mass., unpublished internal report.

code only in that it is preceded by a transformation to the coordinates of an arbitrary Gaussian beam propagating in vacuum. It should be evident, in any case, that such adaptive transformations are restricted to steady-state problems, since for time-dependent problems no single transformation will apply to all time values. To solve time-dependent problems one must employ a Talanov transformation that is optimized to all time values. This optimization is accomplished by a combination of trial and error and intuition.

The splitting algorithm employed in the Four-D code can be written formally as

$$\mathcal{E}^{n+1} = \exp\left(-\frac{i\Delta z}{4k}\nabla_\perp^2\right)\exp\left(-\frac{i\Delta z}{2k}\chi\right)\exp\left(-\frac{i\Delta z}{4k}\nabla_\perp^2\right)\mathcal{E}_n, \quad \text{(A2)}$$

$$\chi = k^2(n^2 - 1) ,$$

where the middle exponential on the right-hand side of Eq. (A2) contains the changes in phase resulting from hydrodynamic changes in density, turbulence, etc. Immediately after this step in the calculation, a quadratic reference phase front is determined and is removed from $\mathcal{E}$ by means of a Talanov transformation and a deflection of the beam coordinates. These operations are carried out as part of the vacuum propagation step. During vacuum propagation the solution is advanced by solving

$$2ik\frac{\partial\mathcal{E}}{\partial z} = \nabla_\perp^2\mathcal{E} . \quad \text{(A3)}$$

Equation (A1) can be written

$$\langle x_i\rangle = \frac{1}{P}\int dx_1\, dx_2\, x_i|\mathcal{E}(x_1,x_2,z)|^2 , \quad \text{(A4a)}$$

$$\langle x_i^2\rangle = \frac{1}{P}\int dx_1\, dx_2\, x_i^2|\mathcal{E}(x_1,x_2,z)|^2 , \qquad i = 1, 2 \quad \text{(A4b)}$$

where P is the beam power given by

$$P = \int dx_1\, dx_2\, |\mathcal{E}(x_1,x_2)|^2 . \quad \text{(A5)}$$

By differentiating Eqs. (A4a) and (A4b) with respect to z and making use of the Fresnel equation (A3), one obtains the following relations:

$$\frac{\partial}{\partial z}\langle x_i^2\rangle = -\frac{2}{kP}\int dx_1\, dx_2 |\mathscr{E}(x_1,x_2,z)|^2\, x_i\, \frac{\partial}{\partial x_i}\,\phi(x_1,x_2,z), \tag{A6a}$$

$$\frac{\partial}{\partial z}\langle x_i\rangle = -\frac{1}{kP}\int dx_1\, dx_2 |\mathscr{E}(x_1,x_2,z)|^2\, \frac{\partial}{\partial x_i}\,\phi(x_1,x_2,z)\ , \tag{A6b}$$

where the phase $\phi(x_1, x_2, z)$ is defined by

$$\phi(x_1,x_2,z) = \mathrm{Im}[\ln \mathscr{E}(x_1,x_2,z)]\ . \tag{A6c}$$

In k-space one can similarly derive

$$\frac{\partial}{\partial z}\langle x_i\rangle = \frac{1}{kP}\iint d\kappa_1\, d\kappa_2\, \kappa_i |\tilde{\mathscr{E}}(\kappa_1,\kappa_2,z)|^2 = \frac{\langle \kappa_i\rangle}{k}\ , \tag{A7a}$$

$$\frac{\partial}{\partial z}\langle x_i^2\rangle = -\frac{2}{kP}\,\mathrm{Im}\iint d\kappa_1\, d\kappa_2\, \kappa_i |\tilde{\mathscr{E}}(\kappa_1,\kappa_2,z)|^2 \times \frac{\partial}{\partial \kappa_i}\,\psi(\kappa_1,\kappa_2,z)\ , \tag{A7b}$$

where $\tilde{\mathscr{E}}(\kappa_1,\kappa_2,z)$ is the Fourier transform of $\mathscr{E}(x_1,x_1,z)$, and

$$\psi(\kappa_1,\kappa_2,z) = \mathrm{Im}[\ln \tilde{\mathscr{E}}(\kappa_1,\kappa_2,z)]\ . \tag{A8}$$

We now wish to determine a phase front that will preserve the following conditions:

$$\frac{\partial}{\partial z}\langle x_i\rangle = 0\ , \tag{A9a}$$

$$\frac{\partial}{\partial z}\langle (x - \langle x_i\rangle)^2\rangle = 0\ , \qquad i = 1,\ 2. \tag{A9b}$$

Equation (A9b) is equivalent to

$$\frac{\partial}{\partial z}\langle x_i^2\rangle - 2\langle x_i\rangle \frac{\partial}{\partial z}\langle x_i\rangle = 0. \tag{A9c}$$

From Eqs. (A9) and (A6) one obtains

$$\frac{\partial}{\partial z}\langle x_i\rangle = -\frac{i}{k}\left\langle \frac{\partial}{\partial x_i}\phi \right\rangle = 0 , \tag{A10a}$$

$$\frac{\partial}{\partial z}\langle x_i^2\rangle = -\frac{i}{k}\left\langle x_i \frac{\partial}{\partial x_i}\phi \right\rangle = 0 . \tag{A10b}$$

Thus the reference phase front must satisfy

$$\left\langle \frac{\partial}{\partial x_i}\phi \right\rangle = 0 , \tag{A11a}$$

$$\left\langle (x_i - \langle x_i\rangle) \frac{\partial}{\partial x_i}\phi \right\rangle = 0 . \tag{A11b}$$

Let us define a new phase variable:

$$\phi'(x_1,x_2,z_{n+\frac{1}{2}}) = \phi_0(x_1,x_2,z_{n+\frac{1}{2}}) + \sum_{i=1}^{2} [\alpha_i(x_i - \langle x_i\rangle)^2 + \beta_i(x_i - \langle x_i\rangle)] , \tag{A12}$$

where $\phi_0(x_1,x_2,z_{n+\frac{1}{2}})$ represents the phase $\phi(x_1,x_2,z_{n+\frac{1}{2}})$ at $z_{n+\frac{1}{2}}$ before the vacuum propagation operator has been applied, and where α_i and β_i are determined so as to make conditions (A11a) and (A11b) hold for the phase front $\phi'(x_1,x_2,z_{n+\frac{1}{2}})$. From Eq. (A11a) we obtain

$$\left\langle \frac{\partial}{\partial x_i}\phi'(x_1,x_2,z_{n+\frac{1}{2}}) \right\rangle = 2\alpha_i \langle x_i - \langle x_i\rangle\rangle + \beta_i + \left\langle \frac{\partial}{\partial x_i}\phi_0(x_1,x_2,z_{n+\frac{1}{2}}) \right\rangle \tag{A13}$$

or

$$\beta_i = -\left\langle \frac{\partial}{\partial x_i}\,\phi_0 \right\rangle = \frac{\langle K_x \rangle}{k} \quad .$$

From (A11b) we obtain

$$\left\langle (x_i - \langle x_i \rangle)\,\frac{\partial}{\partial x_i}\,\phi'(x_1, x_2, z_{\eta+\frac{1}{2}}) \right\rangle = 2\alpha_i \left\langle (x_i - \langle x_i \rangle)^2 \right\rangle + \beta_i \langle x_i - \langle x_i \rangle \rangle = 0$$

or

$$\alpha_i = \frac{\left\langle (x_i - \langle x_i \rangle)\,\dfrac{\partial \phi_0}{\partial x_i} \right\rangle}{2\left\langle (x_i - \langle x_i \rangle)^2 \right\rangle}, \qquad i = 1, 2 \,. \tag{A14}$$

Equations (A13) and (A14), which determine the desired reference phase-front parameters (A12), can be shown to be completely equivalent to the relations used by Bradley and Hermann.[A1]

If the optimal phase front ϕ' is now substituted for the original phase front ϕ_0 at $z_{\eta+\frac{1}{2}}$, the phase increment

$$\phi_0 - \phi' = -\sum_{i=1}^{2} \left[\alpha_i (x_i - \langle x_i \rangle)^2 + \beta_i (x_i - \langle x_i \rangle)\right] \tag{A15}$$

must be compensated for in some way in order to preserve the original field. The quadratic contribution in (A15) is compensated for by a generalized Talanov transformation, which involves a rescaling of $\mathcal{E}$, the mesh, and Δz, according to

$$\mathcal{E}(x,y,z) = \frac{1}{\left(1 - \dfrac{\Delta z}{z_x}\right)^{\frac{1}{2}} \left(1 - \dfrac{\Delta z}{z_x}\right)^{\frac{1}{2}}} \times \mathcal{E}\left(\frac{x}{1 - \dfrac{\Delta z}{z_x}}, \frac{z}{1 - \dfrac{\Delta z}{z_y}}, z\right) \exp\left[i\,\frac{k}{2}\left(\frac{x^2}{z_x - \Delta z} + \frac{y^2}{z_y - \Delta z}\right)\right], \tag{A16a}$$

where

$$\tilde{\mathcal{E}}(\kappa_x,\kappa_y,z) = \tilde{\mathcal{E}}(\kappa_x,\kappa_y,z-\Delta z)\,\exp\left[i\left(\frac{z_1\kappa_x^2}{2k} + \frac{z_2\kappa_y^2}{2k}\right)\right], \quad \text{(A16b)}$$

$$z_1 = \frac{z}{1-(\Delta z/z_x)} \quad , \quad \text{(A16c)}$$

$$z_2 = \frac{z}{1-(\Delta z/z_y)} \quad . \quad \text{(A16d)}$$

The generalized focal lengths z_x and z_y are determined by combining the reciprocals of the current focal lengths,

$$z_x^c = 2\alpha_1/k \ , \quad \text{(A17a)}$$

$$z_y^c = 2\alpha_2/k \ , \quad \text{(A17b)}$$

with those remaining from previous propagation steps (see argument of exponential in Eq. (A16a)).

The linear term in (A15) corresponds to solving Eq. (A3) in a coordinate system that has been rotated in x-y-z space. If this rotation is assumed to be small, it can be represented by a net deflection in the x and y coordinates given by

$$\delta x = -(\beta_1/k)z \ , \quad \text{(A18a)}$$

$$\delta y = -(\beta_2/k)z \ . \quad \text{(A18b)}$$

The contribution $\Sigma_i\ \beta_i(x_i - \langle x_i \rangle)$ must also be added to ϕ_0 before the vacuum propagation calculation, but this operation may correspond to a translation of the Fourier transform $\tilde{\mathcal{E}}(\kappa_x,\kappa_y)$ by a nonintegral number of steps on the

k-space mesh. In order to avoid this, $\beta_1/\Delta\kappa_x$ and $\beta_2/\Delta\kappa_y$ are both rounded off to the nearest integer, and $\mathscr{E}(\kappa_x,\kappa_y)$ is then translated on its mesh in the x and y directions by the corresponding number of steps.

The numerical implementation of Eqs. (A13) and (A14) requires the following computations, where j and k represent the numerical coordinates of the mesh points:

$$E = \sum_{j,k} |E_{jk}|^2 ,$$

$$\langle x \rangle = \frac{1}{E} \sum_{j,k} x_j |\mathscr{E}_{jk}|^2 ,$$

$$\left\langle (x - \langle x \rangle)^2 \right\rangle = \frac{1}{E} \sum_{j,k} x_j^2 |\mathscr{E}_{jk}|^2 - x^2 , \tag{A19}$$

$$\beta_x = \frac{\sum_{j,k} \kappa_j |\tilde{\mathscr{E}}_{jk}|^2}{\sum_{j,k} |\tilde{\mathscr{E}}_{jk}|^2} ,$$

$$\left\langle \frac{\partial \phi}{\partial x} \right\rangle = (2\Delta x E)^{-1} \operatorname{Im} \sum_{j,k} (\mathscr{E}_{jk} - \mathscr{E}_{j-1,k})(\mathscr{E}^*_{jk} + \mathscr{E}^*_{j-1,k}) ,$$

$$\left\langle (x - \langle x \rangle) \frac{\partial \phi}{\partial x} \right\rangle = (2\Delta x E)^{-1} \times \operatorname{Im} \sum_{j,k} x_j (\mathscr{E}_{jk} - \mathscr{E}_{j-1,k})(\mathscr{E}^*_{jk} + \mathscr{E}^*_{j-1,k}) - \langle x \rangle \left\langle \frac{\partial \phi}{\partial x} \right\rangle .$$

The computations involving the variable y are carried out in an analogous manner. In the calculation of the average phase derivative, the phase derivative is monitored at each point and limited in magnitude to a fraction of π. This prevents rapid phase fluctuations near the mesh boundary, where intensities may be weak, from contributing disproportionately to the average.

Appendix B: An Adaptive Algorithm for Selecting the Axial Space Increment

It is desirable to have the code select the next axial space increment Δz at a given axial position on the basis of requirements for numerical accuracy in the solution of the wave equation. The numerical accuracy of the vacuum propagators in the symmetrically split solution operator,

$$\mathcal{E}^{n+1} = \exp\left(-\frac{i\Delta z}{4k}\ \nabla_\perp^2\right) \exp\left(-\frac{i\Delta z}{2k}\ \bar{\chi}\right) \exp\left(-\frac{i\Delta z}{4k}\ \nabla_\perp^2\right) \mathcal{E}^n, \quad \text{(B1)}$$

is independent of Δz if the solution is based on a discrete Fourier transform. The imposition of the phase front,

$$\Delta\phi = -\frac{\Delta z \bar{\chi}}{2k}\ , \quad \text{(B2)}$$

at $z = z_{n+\frac{1}{2}}$, which is equivalent to passing the beam through a lens, will make the solution meaningless if any of the transverse zone-to-zone phase differences violate

$$|\delta_x(\Delta\phi)| \lesssim f\pi\ , \quad \text{(B3)}$$

$$|\delta_y(\Delta\phi)| \lesssim f\pi\ ,$$

$$0 < f \leq 1\ .$$

It will always be necessary then to restrict the value of Δz so that conditions (B3) are met. While violating conditions (B3) destroys the numerical integrity of the solution, satisfying them does not completely guarantee accuracy, since errors can also result from the noncommutation of $\nabla_\perp^2$ and $\bar{\chi}$, and from upgrading $\bar{\chi}$ too infrequently. These errors must be controlled externally by inputting a maximum allowable value of Δz.

In practice, part of the effect of the phase front (B2) is removed by the adaptive lens transformation. It would therefore be too restrictive to limit Δz on the basis of conditions (B3). As an alternative one can restrict the value of Δz so as to control transverse gradients in the phase variable

$$\theta = \sum_{i=1}^{2} \alpha_i (x_i - \langle x_i \rangle_I)^2 - \frac{k}{2} \frac{\partial \varepsilon}{\partial \rho} \Delta z^n \rho_1 \ , \tag{B4}$$

which is that part of the nonlinear phase front at $z_{n+\frac{1}{2}}$ that cannot be removed by the adaptive lens transformation. The next spacial increment Δz^{n+1} is then chosen in terms of the current value Δz^n by means of the relation

$$\Delta z^{n+1} = \frac{f \Delta z^n \pi}{\max \{ |\theta_{j,k+1} - \theta_{jk}|, \ |\theta_{j+1,k} - \theta_{jk}| \}_{I_{jk} \geq f' I_{\max}}} \ . \tag{B5}$$

The arguments of the maximum function in the denominator of expression (B5) are restricted to those mesh points where the intensity is greater than a certain fraction f' of the maximum intensity. The final value of Δz^{n+1}, however, must satisfy the additional constraints:

$$0.8 \Delta z^n \leq \Delta z^{n+1} \leq 1.2 \ \Delta z^n \ , \tag{B6}$$

$$\Delta z_{\min} < \Delta z^{n+1} \leq \Delta z_{\max} \ , \tag{B7}$$

$$\Delta z^{n+1} \leq \frac{z_T \sqrt{2 f_D}}{\sqrt{2 f_D} + \dfrac{z_T}{k \left[\left\langle (x - \langle x \rangle)^2 \right\rangle + \left\langle (y - \langle y \rangle)^2 \right\rangle \right]}} \ , \tag{B8}$$

with (B6) taking precedence over (B5), (B7) over (B6), and (B8) over (B7). In Eq. (B8), $f_D \approx 0.005$ is an input fraction and $z_T = \min(|z_x|, \ |z_y|)$. Condition (B8) is designed to reduce Δz near a focus, where the geometric-optics scaling of the mesh by the Talanov transformation may result in an excessive shrinkage of the mesh. By updating the Talanov transformation sufficiently often, one can usually avoid a geometric-optics catastrophe.

The adaptive z-step algorithm just described adds greatly to the convenience of running problems; it often improves problem running time, and avoids large nonlinear phase changes that can invalidate the calculation. It should not, however, be regarded as a panacea. For sufficiently high beam power and strong enough thermal blooming, the criteria (B5)-(B8) can

be satisfied and yet the problem still goes bad. In such cases, large non-quadratic transverse zone-to-zone phase differences can accumulate over many z-steps.

Appendix C: Treatment of Multiline Absorption

The treatment of multiline absorption in the Four-D code follows the method of Hogge.[C1] The basic assumptions are that all lines operate with the same transverse mode structure in the laser and that the line frequencies are near enough to each other so that the field for each line will be affected in the same way by the atmospheric density distribution. Thus at each position z, for the ith line $\mathcal{E}_i(z) \propto \mathcal{E}(z)$, and the field will be completely characterized by the fractions $f_i(z)$ of the total power $P(z)$ that are found in each line.

At $z = 0$ one has

$$P_i(0) = f_i(0)\, P(0)\ , \tag{C1}$$

and at position z

$$\begin{aligned} P_i(z) &= P_i(0)\ e^{-\alpha_i z}\ , \\ P(z) &= \sum_i P_i(z) = P(0) \sum_i f_i(0)\ e^{-\alpha_i z}\ , \\ f_i(z) &= \frac{f_i(0)\ e^{-\alpha_i z}}{\sum_i f_i(0)\ e^{-\alpha_i z}}\ . \end{aligned} \tag{C2}$$

Thus,

$$I_i(z) = f_i(z)\ I(z), \tag{C3}$$

and the energy-deposition rate per unit volume is given by

C1. C. B. Hogge, "A Comparison of Several High Energy Laser Systems with Emphasis on Propagation Aspects," in *Laser Digest*, AFWL-TR-75-140 (May 1975).

$$\sum_i \alpha_i I_i(z) = I(z) \sum_i \alpha_i f_i(z) \quad , \tag{C4}$$

in which

$$\sum_i \alpha_i f_i(z) = \bar{\alpha}(z) \tag{C5}$$

can be interpreted as an average cross section throughout the calculation.

Tables C1 and C2 show values for $\bar{\alpha}(z)$ as a function of z for the DF line data found in Ref. C2. Clearly, for DF the effect of including all line absorption details leads to a very small correction even at 10 km.

Table C1. Line-by-line absorption-coefficient data.

Line ID	Line frequency (cm^{-1})	Fraction of total power $z = 0$	Fraction of total power $z = 10$ km	Absorption coefficient (km^{-1})
4-3,7	—	0.01040	0.01006	0.06000
3-2,10	2496.77	.00590	.00636	.04920
4-3,6	—	.02130	.02060	.06000
3-2,9	2521.81	.01330	.01632	.03620
4-3,5	—	.01040	.01006	.06000
3-2,8	2546.42	.04750	.05401	.04380
3-2,7	2570.51	.06380	.06108	.06100
2-1,10	2580.10	.00910	.00813	.06790
3-2,6	2594.25	.08970	.11944	.02800
2-1,9	2605.80	.03180	.03786	.03920
3-2,5	2617.44	.05630	.07960	.02200
2-1,8	2631.06	.08450	.10460	.03530
2-1,7	2655.85	.09040	.05918	.09900
2-1,6	2680.17	.13040	.12864	.05800
1-0,9	2691.61	.03230	.02557	.08000
2-1,5	2703.99	.04000	.05300	.02850
1-0,8	2717.54	.06440	.03629	.11400
1-0,7	2743.00	.08740	.08434	.06020
1-0,6	2767.97	.08370	.06178	.08700
1-0,5	2792.43	0.02740	0.02310	0.07370

C2. R. K. Long, F. S. Mills, and G. L. Trusty, *Calculated Absorption Coefficients for DF Laser Frequencies*, Ohio State University Electro-Science Laboratory, Rept. RADC-TR-73-389.

Table C2. Mean absorption coefficient as a function of distance.

Propagation distance (km)	Mean absorption coefficient (km^{-1})	Remaining power fraction in beam
0	0.06001	1.00000
1	0.05931	0.94209
2	0.05862	0.88815
3	0.05793	0.83787
4	0.05726	0.79097
5	0.05660	0.74720
6	0.05594	0.70632
7	0.05530	0.66811
8	0.05467	0.63236
9	0.05404	0.59891
10	0.05343	0.56758

Appendix D: Characterization of Nondiffraction-Limited Beams

In the absence of detailed *a priori* information regarding the exact mode content of a beam, several models of nondiffraction-limited beam behavior can be applied with the Four-D code.

The simplest of these, which requires no special coding, is wavelength scaling, wherein the laser wavelength is multiplied by a number equal to the beam quality factor. Wavelength scaling gives the correct vacuum peak intensity, although it may incorrectly represent the vacuum focal-spot size. It represents, in any case, a prescription whose accuracy needs to be evaluated *ad hoc* for each specific application. While it has been useful in a variety of applications, it does not properly account for discrepancies between calculations and stagnation blooming experiments in vertical absorption cells.[D1]

Agreement between measured data and calculations for these experiments is improved, on the other hand, by adding spherical aberration to the initial beam in such a way that the vacuum focal-spot size is correctly reproduced (see Fig. D1). The spherical aberration contribution to the initial phase can be represented as

$$\phi^{SA} = \frac{2\pi A}{\sigma_x^2}\,(x^2 + y^2)^2 \quad , \tag{D1}$$

where A represents the number of waves of aberration at radius σ_x.

A third model of nondiffraction-limited behavior is due to Hogge *et al.*[D2] This model is based on the assumption that the initial beam can be represented by

$$\mathcal{E}(x,y,0) = \mathcal{E}_0(x,y)\; e^{i\phi(x,y)} \quad , \tag{D2}$$

where the phase aberration $\phi(x,y)$ is a Gaussian random variable, arising from laser-medium inhomogeneities, mirror imperfections, etc. If it is assumed that the correlation function for phase fluctuations is

D1. J. A. Fleck, Jr., J. R. Morris, and M. D. Feit, *Time-Dependent Propagation of High Energy Laser Beams Through the Atmosphere*, Lawrence Livermore Laboratory, Rept. UCRL-51826 (1975).

D2. C. B. Hogge, R. R. Butts, and M. Burlakoff, *Appl. Opt.* 13, 1065 (1974).

$$C_\phi(r) = \sigma_\phi^2 \exp\left(-\frac{r^2}{2l_0^2}\right) \tag{D3}$$

where $r^2 = x^2 + y^2$, σ_ϕ^2 is the variance of ϕ, and l_0 is the phase coherence length, then the spectrum of the phase fluctuations is given by

$$\tilde{C}_\phi(\underline{k}_\phi) = \frac{\sigma_\phi^2 l_0^2}{2\pi} \exp\left(-\frac{l_0^2 k_\phi^2}{2}\right). \tag{D4}$$

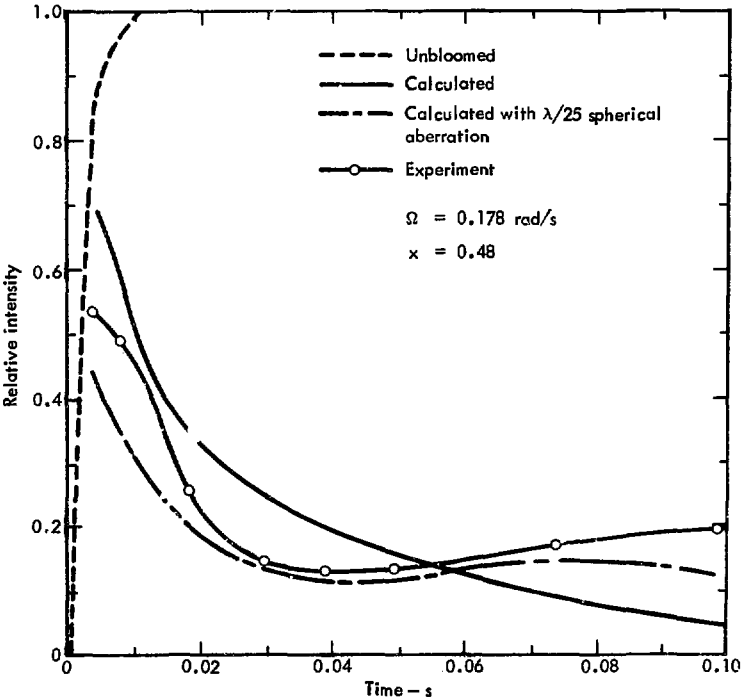

Fig. D1. Intensity on target after passing through stagnation zone. Comparison between experiment and calculation with and without spherical aberration. (Data from P. J. Berger, F. G. Gebhardt, and D. Smith, *Thermal Blooming Due to a Stagnation Zone in a Slewed Beam*, United Aircraft Research Laboratory, East Hartford, Conn., Rept. N921724-12 (1974).)

Using the method of phase screens, one can obtain the Fourier transform of the phase $\phi(x,y)$ to be used in Eq. (D1) in the following form:

$$\phi(\underline{k}_\phi) = \left(\frac{a'(\underline{k}_\phi) + ia''(\underline{k}_\phi)}{\sqrt{2}}\right) \tilde{C}_\phi^{1/2}(\underline{k}_\phi), \tag{D5}$$

where a' and a'' are Gaussian random variables with variance 1, and where

$$\begin{aligned} a'(\underline{k}_\phi) &= a'(-\underline{k}_\phi) , \\ a''(\underline{k}_\phi) &= -a''(-\underline{k}_\phi) . \end{aligned} \tag{D6}$$

Equations (D5) and (D6) were originally included in the Four-D code for simulating turbulence. The phase-screen model of nondiffraction-limited beams utilizes the same subroutines.

The following parameters were the basis of an example for comparing the difference between the wavelength-scaling and the phase-screen models of nondiffraction-limited behavior:

Beam shape	Gaussian
Aperture size, $2a$	80 cm
Range	2.5 km
Absorption coefficient, α	0.07 km^{-1}
Transverse wind speed, v	10 m/s
Focal distance, f	2.5 km
Beam is 2× diffraction limited	
Wavelength, λ	5.7 μm
Scaled wavelength, λ	11.4 μm
Phase correlation length, l_0	5.0 cm
Phase standard deviation, σ_ϕ	1.177 (rad)
Number of phase-screen calculations for ensemble average	10

Table D1 gives a comparison of peak intensities in the focal plane for propagation in vacuum and air. Also included are results for a uniformly illuminated aperture of radius $a_0 = 2a$, which can likewise be used as a model of a 2× diffraction-limited beam.

Table D1. Comparison of peak intensities in the focal plane. Beam propagates in vacuum (linear) and air (nonlinear). Case: Gaussian diffraction-limited beam, a uniformly illuminated aperture (top hat), Gaussian wavelength scaled (2× diffraction limited), and a Gaussian beam with a phase screen adjusted to 2× diffraction limited.

Model	Peak intensity in focal plane (kW/cm^2)
Linear	
Gaussian, λ	63.8
Gaussian, 2λ	15.9
Top hat	17.4
Phase screen	17.7
Nonlinear	
Gaussian, 2λ	5.94
Top hat	5.47
Phase screen	3.03

The nondiffraction-limited beams all give roughly one quarter of the focal-plane intensity of the diffraction-limited beam when propagated in vacuum. For propagation in a real absorbing atmosphere both the scaled wavelength and the top-hat beam calculations result in twice the peak intensity of the phase-screen model calculation, which is based on an ensemble average taken over 10 independent phase screens. Figures D2 and D3 show respectively the beam intensity as a function of position along the x-axis and along a line parallel to the y-axis passing through the point of maximum intensity along the x-axis for the wavelength-scaled beam. Figures D4 and D5 show the same plots

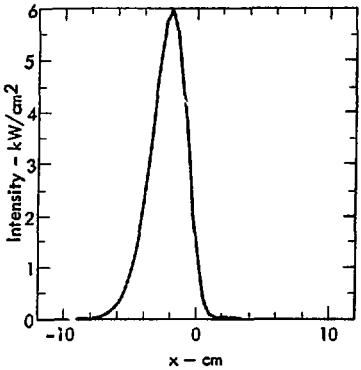

Fig. D2. Wavelength scaling for 2× diffraction-limited beam. Intensity on target as a function of x along x-axis.

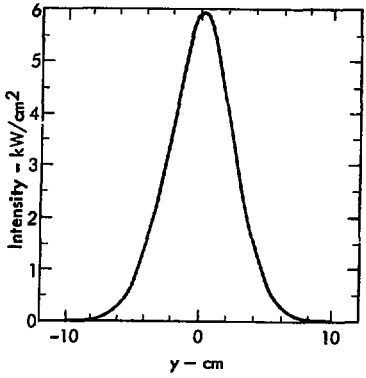

Fig. D3. Wavelength scaling for 2× diffraction-limited beam. Intensity on target as a function of y along a line parallel to y-axis and passing through point of maximum intensity along the x-axis.

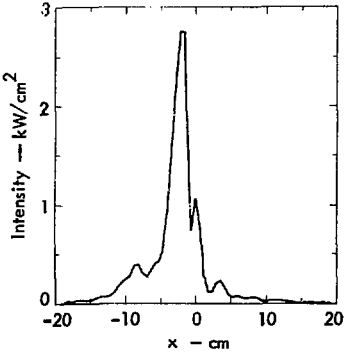

Fig. D4. Phase-screen model of 2× diffraction-limited beam averaged over 10 independent realizations. Intensity on target as a function of x along x-axis.

for the ensemble averaged phase-screen calculation. In the case of the wavelength-scaled calculation, thermal blooming leads primarily to a broadening of the beam. In the phase-screen calculation, thermal blooming is accompanied by considerable scattering of energy to the far reaches of the mesh.

From these calculations it can be concluded that different models of nondiffraction-limited beam behavior can lead to qualitatively as well as quantitatively different thermal-blooming behavior. Which

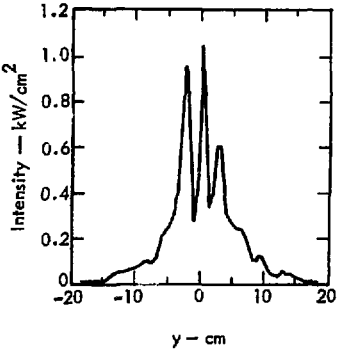

model is best must be determined for each specific situation. In the last analysis there is no substitute for an accurate experimental characterization of the beam for each specific laser.

Fig. D5. Phase-screen model of 2× diffraction-limited beam averaged over 10 independent realizations. Intensity on target as a function of y along a line parallel to y-axis and passing through point of maximum intensity along the x-axis.

GS/11/mm/edas/1a